mathematics

MDPI

Article

An Analytical Framework for Assessing the Unsaturated Bearing Capacity of Strip Footings under Transient Infiltration

Sheng Xu and De Zhou *

School of Civil Engineering, Central South University, Changsha 410075, China; 214811046@csu.edu.cn
* Correspondence: 210026@csu.edu.cn

Abstract: The evaluation of the bearing capacity of strip footings generally assumes that the soil is either dry or fully saturated, which contradicts the actual condition in nature where the soil is often in a partially saturated state. Furthermore, infiltration has a significant impact on the shear strength of the soil. Following the upper bound theory of the limit analysis, this article provides a theoretical framework for assessing the bearing capacity under transient flow with linear variation in infiltration intensity for the first time. Firstly, the closed form of suction stress under linear transient infiltration is derived using Laplace transform and introduced into the Mohr–Coulomb criterion. A discrete failure mechanism with fewer variables and higher accuracy is provided to ensure kinematic admissibility. The upper bound solution for bearing capacity is obtained by solving the power balance equation. The present results are compared with results from the published literature and the finite element, confirming the validity and superiority of the theoretical framework provided. A parametric analysis is also conducted on three hypothetical soil types (fine sand, silt, and clay), and the results show that unsaturated transient infiltration has a positive influence on increasing the foundation bearing capacity. The magnitude of the influence is comprehensively controlled by factors such as soil type, saturated hydraulic conductivity, infiltration intensity, infiltration time, and water table depth. The increase in bearing capacity due to unsaturated transient infiltration can be incorporated into Terzaghi's equation as a separate component presented in tabular form for engineering design purposes.

Keywords: bearing capacity; strip footings; upper bound; unsaturated soils; transient infiltration

MSC: 49-06

Citation: Xu, S.; Zhou, D. An Analytical Framework for Assessing the Unsaturated Bearing Capacity of Strip Footings under Transient Infiltration. *Mathematics* **2023**, *11*, 3480. https://doi.org/10.3390/math11163480

Academic Editor: Smirnov Nikolay Nikolaevich

Received: 18 July 2023
Revised: 5 August 2023
Accepted: 9 August 2023
Published: 11 August 2023

1. Introduction

For decades, the classical problem of assessing the bearing capacity of strip footings has been extensively studied in conjunction with various practical engineering factors such as soil types, characteristics of loads, seismic forces, and seepage, as well as reinforcement with steel bars. A variety of methods have been used in this research, including experimental testing, numerical simulation, limit equilibrium analysis, limit analysis, and probabilistic analysis [1–5]. Among these methods, limit analysis has gained widespread application due to its computational simplicity and ability to provide reliable theoretical solutions while considering various influencing factors.

Calculating the bearing capacity of a foundation using analytical methods requires first determining its failure mechanism. Initially, failure mechanisms were classified as Prandtl [6] and Hill [7] mechanisms based on whether the foundation's roughness was considered. Both mechanisms have a plastic zone bounded by a logarithmic spiral, but the Prandtl mechanism, which takes into account foundation friction, yields a higher bearing capacity. Building upon these concepts, Michalowski [8] proposed a method to model the failure mechanism with a large number of triangular rigid blocks, forming a multi-block failure mechanism. His approach involved minimizing the failure load with

respect to all possible kinematically admissible directions at the base of each selected block, thus introducing multiple variables. Subsequently, Soubra [9] and Zhu [10] used Michalowski's method. Soubra [9] obtained the upper-bound solution for seismic bearing capacity using the multi-block mechanism, while Zhu [10] combined the mechanism with the limit equilibrium method. To simplify the optimization process for the multi-block mechanism, Kumar [11] assumed that all the triangular blocks' outer edges still followed a logarithmic spiral. This idea was used by Kang et al. [12] in their analysis of the bearing capacity of rock foundations. However, in Kang et al.'s mechanism, the triangular blocks no longer shared the same logarithmic spiral, but each triangle's base corresponds to a separate logarithmic spiral.

Research on foundation bearing capacity often assumes strict conditions of extreme saturation, that is, either fully saturated or completely dry. However, soils in the natural environment are often in a partially saturated state due to factors such as rainfall, evaporation, groundwater fluctuations, and topography. Previous studies have shown that the presence of gas or gas–water interfaces and capillary forces in unsaturated soils greatly enhance their shear strength [13,14]. In order to evaluate the mechanical properties of soils under realistic conditions, Bishop [15], Fredlund et al. [16], and Vanapalli et al. [17] proposed different effective stress equations based on matric suction. However, Professor Lu and his colleagues [18,19] pointed out the limitations of using matric suction in geotechnical problems and introduced the concept of suction stress as a fundamental component for assessing the shear strength of unsaturated soils. Suction stress can provide a reasonable explanation for the properties of unsaturated soils, climate variations (infiltration/evaporation), and fluid flow behavior. Moreover, it can unify the solutions for unsaturated and saturated soils. By using the effective stress expression based on suction stress, some classical geotechnical problems such as slope stability, tunnel face stability, and earth pressure have obtained more accurate solutions [20–22]. Considering the influence of suction stress, the bearing capacity of the foundation can be assessed more optimistically. It is worth noting that most of the relevant literature is still based on Terzaghi's equation. Vahedifard and Robinson [23] and Tang et al. [24] made different extensions to Terzaghi's bearing capacity equation, considering the non-linear relationship between bearing capacity and suction stress. Du et al. [25] and Xu and Zhou [26] obtained upper-bound solutions for the bearing capacity under seepage, which still applied the original Terzaghi's equation. Roy and Chakraborty [27], using the Hill mechanism, added the contribution of suction stress to bearing capacity as a separate item to Terzaghi's equation.

Research on the bearing capacity of shallow foundations under unsaturated conditions, including the literature mentioned above, typically considers one-dimensional steady-state flow. In the case of steady-state flow, it is assumed that the soil moisture movement reaches an equilibrium state, where the input and output rates of water are equal. However, in practical engineering, water flow rates and hydraulic head vary over time, and the strength of the soil exhibits significant spatiotemporal variations. Events such as rainfall, snowmelt, and changes in groundwater levels are typical examples of transient infiltration. During the gradual development of transient infiltration, the unsaturated components of shear strength change with time and depth. Recently, climate change has led to more extreme rainfall events [28]. Some scholars incorporated the one-dimensional transient flow analytical solution developed by Sriastava and Yeh [29] into their research on geotechnical-related problems [30,31]. The slip line method and lower bound finite element method were used by Tan and Vanapalli [32,33] and Fathipour et al. [2] to extend the calculation for foundation bearing capacity to unsaturated soil under transient flow conditions, respectively. However, these studies under transient flow assume that the infiltration intensity is constant, which is clearly not realistic. Taking rainfall as an example, its intensity tends to fluctuate significantly over time. Among them, rainfall with linear intensity changes is the most common, including advanced-peak type, delayed-peak type, and uniform type. No researchers have yet studied the bearing capacity response under such conditions.

This paper aims to obtain more realistic solutions for the bearing capacity of strip footings under unsaturated transient infiltration. Assuming that the infiltration intensity varies linearly with time, analytical solutions for the suction stress and apparent cohesion under three types of transient infiltration are derived. The modified M-C criterion with apparent cohesion is introduced into the theoretical framework of upper bound limit analysis [34–36]. A discrete multi-block mechanism with fewer variables and higher accuracy is proposed for the numerical integration of apparent cohesion. After verifying the correctness of the present results using the geotechnical analysis software *Geo-studio*, three hypothetical soils (fine sand, silt, and clay) are selected for parametric analysis and collapse range analysis. The increase in bearing capacity due to the transient infiltration is incorporated as a separate item in Terzaghi's equation, which is presented in tabular form for ease of use.

2. Apparent Cohesion Subject to Transient Infiltration

2.1. Suction Stress and Apparent Cohesion

The stress distribution of unsaturated soil is a critical theoretical basis for the design and analysis of strip footings. The effective stress expression based on suction stress proposed by Lu and Likos [18] has been widely applied in the study of stress distribution in unsaturated soils. The unified form is:

$$\sigma' = \sigma - u_a - \sigma^s \tag{1}$$

where σ' = the effective stress, σ = the total stress, u_a = the pore air pressure; and σ^s = the suction stress.

The introduction of suction stress avoids the uncertainty in the effective stress coefficient χ in Bishop's theory. Moreover, the magnitude of the suction stress completely depends on the matrix suction, and the expression is as follows:

$$\sigma^s = \begin{cases} -(u_a - u_w) & \text{if } (u_a - u_w) < 0 \\ -S_e(u_a - u_w) & \text{if } (u_a - u_w) \geq 0 \end{cases} \tag{2}$$

where $(u_a - u_w)$ = matric suction and S_e = effective degree of saturation, which can be obtained with:

$$S_e = \frac{\theta - \theta_r}{\theta_s - \theta_r} \tag{3}$$

where θ, θ_s, and θ_r are the volumetric water content, saturated volumetric content, and residual volumetric water content, respectively. To describe the shear strength characteristics of unsaturated soil, an extended M-C criterion is used, which is defined as:

$$\begin{aligned} \tau_f &= c' + \sigma' \tan \varphi' \\ &= c' + (\sigma - u_a) \tan \varphi' - \sigma^s \tan \varphi' \end{aligned} \tag{4}$$

where τ_f = the strength of the soil and c' and φ' represent the effective cohesion and friction angle, respectively. In general, the additional cohesion caused by suction stress $-\sigma^s \tan \varphi'$ in Equation (4) is called apparent cohesion c_{app}, which means $c_{app} = -\sigma^s \tan \varphi'$. The introduction of apparent cohesion c_{app} unified the approach for treating dry soil and variably saturated soil, which divides the cohesion into two parts in the analysis: apparent cohesion and effective cohesion. Of course, this approach needs to be based on the assumption that the effective shear strength, including c' and φ', is independent of changes in apparent cohesion c_{app} and remains constant during infiltration.

2.2. Analytical Solution for Unsaturated Transient Flow

In homogeneous and isotropic soil layers, the general assumption of seepage in the soil is subject to Darcy's law [37–40]. In that case, the one-dimensional expression of Richard's equation reflecting transient flow is:

$$\frac{\partial \theta(h_m)}{\partial t} = \frac{\partial}{\partial z}\left[k(h_m)\left(\frac{\partial h_m}{\partial z} + 1\right)\right] \tag{5}$$

where t = the time, z = vertical distance from groundwater level, with $z = l$ representing the earth's surface, h_m = suction head, derived from $h_m = -\frac{(u_a - u_w)}{\gamma_w}$, and γ_w = the unit weight of water, generally taking a value of 10 kN/m^3. In order to conveniently obtain the solution for the nonlinear partial differential Equation (5), the volume of water content θ and hydraulic conductivity k are calculated according to Gardner's model [41]:

$$k = k_s e^{\alpha h_m} \tag{6}$$

$$\theta = \theta_r + (\theta_s - \theta_r)e^{\alpha h_m} \tag{7}$$

where k_s = hydraulic conductivity of saturated soils and α is a parameter for unsaturated soils that represents the decrease in hydraulic conductivity and water content as the suction head increases. By substituting Equations (6) and (7) to Equation (5), a linearized partial differential equation system can be obtained, namely:

$$\frac{\alpha(\theta_s - \theta_r)}{k_s}\frac{\partial k(h_m)}{\partial t} = \frac{\partial^2 k(h_m)}{\partial z^2} + \alpha\frac{\partial k(h_m)}{\partial z} \tag{8}$$

To solve this equation, two boundary conditions and an initial condition are required. This article uses a steady seepage field formed by a previous infiltration intensity of q_A the initial state. The two boundary conditions refer to (1) the suction stress h_m at the water table equals h_0, with $h_0 = 0$. In this case, the initial suction head h_m is linearly distributed in the soil. (2) When $t > 0$, transient infiltration with an intensity of q_B acts on the surface of the foundation ($z = l$).

$$q_B = q_0 + mt \tag{9}$$

where q_0 = initial infiltration intensity and m = infiltration intensity variation coefficient, where $m = 0$ represents uniform infiltration, $m > 0$ represents delayed-peak infiltration, and $m < 0$ represents advanced-peak infiltration, as shown in Figure 1. Herein, several parameters are introduced:

$$K = \frac{k(\psi)}{k_s}, Q_A = \frac{q_A}{k_s}, Q_0 = \frac{q_0}{k_s}, Z = \alpha z, L = \alpha l, T = \frac{\alpha k_s t}{\theta_s - \theta_r}, M = \frac{m(\theta_s - \theta_r)}{\alpha {k_s}^2}$$

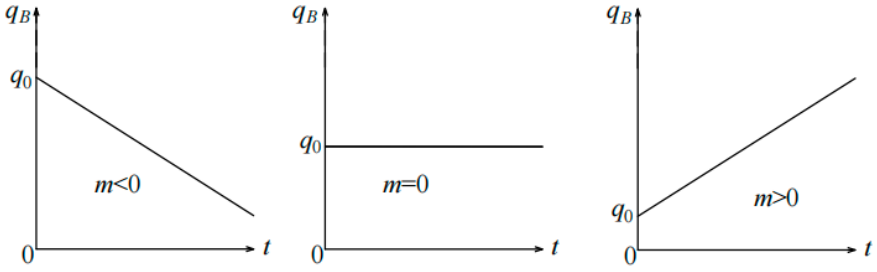

Figure 1. Finite element model for a foundation under rainfall infiltration.

In this way, the control Equation (8) can be simplified as:

$$\frac{\partial K}{\partial T} = \frac{\partial^2 K}{\partial Z^2} + \frac{\partial K}{\partial Z} \tag{10}$$

The boundary conditions and initial conditions can be recorded as:

$$\begin{cases} K(Z,\ 0) = Q_{\mathrm{A}} - (Q_{\mathrm{A}} - 1)\mathrm{e}^{-Z} \\ \left[\frac{\partial K}{\partial Z} + K\right]_{Z=L} = Q_{\mathrm{B}} \\ K(0,\ T) = 1 \end{cases} \tag{11}$$

An analytical solution for the normalized hydraulic conductivity K is obtained using Laplace forward and inverse transformations, with a detailed derivation process referred to Sriastava and Yeh [29] and Qin et al. [42].

$$K = Q_{\mathrm{A}} - (Q_{\mathrm{A}} - 1)\mathrm{e}^{-Z} + \mathrm{e}^{\frac{L-Z}{2}}\left[MG(t) + (Q_0 - Q_{\mathrm{A}})F(t)\right] \tag{12}$$

where

$$\begin{aligned} G(t) = {} & 2Z\cosh(\tfrac{Z}{2})\mathrm{e}^{-\frac{L}{2}} + \sinh(\tfrac{Z}{2})\left[2T\mathrm{e}^{-\frac{L}{2}} - 4e^{-L}\cosh(\tfrac{L}{2}) - 2L\mathrm{e}^{-\frac{L}{2}}\right] \\ & + \sum_{n=1}^{\infty} \frac{16\cos^2(\lambda_n L)\sin(\lambda_n Z)\sin(\lambda_n L)\mathrm{e}^{(-\lambda_n^2 - \frac{1}{4})T}}{1 + \frac{L}{2} + 2\lambda_n^2 L} \end{aligned} \tag{13}$$

$$F(t) = \mathrm{e}^{-\frac{(L-Z)}{2}} - \mathrm{e}^{-\frac{(L+Z)}{2}} + \sum_{n=1}^{\infty} \frac{-4\sin(\lambda_n Z)\sin(\lambda_n L)\mathrm{e}^{(-\lambda_n^2 - \frac{1}{4})T}}{1 + \frac{L}{2} + 2\lambda_n^2 L} \tag{14}$$

and λ_n refers to the nth positive root of the following pseudo-periodic characteristic equation:

$$\tan(\lambda_n L) + 2\lambda_n = 0 \tag{15}$$

For the uniform type of transient infiltration, substituting M = 0 into Equation (12) yields an expression for K in this case, i.e.,:

$$K = Q_0 - (Q_0 - 1)\mathrm{e}^{-Z} - 4(Q_0 - Q_{\mathrm{A}})\mathrm{e}^{\frac{L-Z}{2}}\mathrm{e}^{-\frac{T}{4}}\sum_{n=1}^{\infty} \frac{\sin(\lambda_n Z)\sin(\lambda_n L)\mathrm{e}^{-\lambda_n^2 T}}{1 + L/2 + 2\lambda_n^2 L} \tag{16}$$

The saturation degree S_e, water head h_m, suction stress σ^s, and apparent cohesion c_{app} can all be expressed as functions of K:

$$S_e = K \tag{17}$$

$$u_a - u_w = -\frac{\gamma_w \ln K}{\alpha} \tag{18}$$

$$\sigma^s = \frac{\gamma_w K \ln K}{\alpha} \tag{19}$$

$$c_{app} = -\frac{\gamma_w K \ln K}{\alpha}\tan\varphi' \tag{20}$$

3. Bearing Capacity of Strip Footings on Unsaturated Soils

3.1. Problem Description and Solution Method

As shown in Figure 2, a rigid strip footing with a width of B is resting over homogeneous, isotropic, saturated soils, and the burial depth of the water table is l. In order to simplify the bearing capacity analysis, some basic assumptions are required: (1) the load on the foundation is vertical and concentric; (2) the soil in the damaged area follows the modified Mohr–Coulomb (M-C) failure criterion; (3) the interface between the foundation material and the soil is smooth to achieve conservative estimation; and (4) the water table exceeds the damaged area and is parallel to the ground.

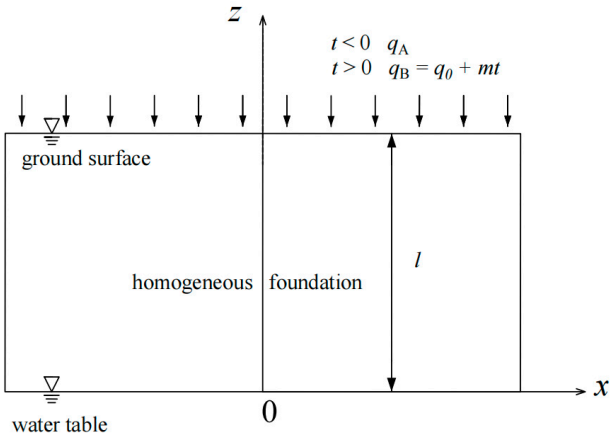

Figure 2. Transient seepage in the homogeneous foundation.

The upper-bound method of limit analysis has been widely used in classic soil mechanics problems such as slope stability analysis, tunnel stability analysis, and foundation bearing capacity calculation [43–49]. No matter how complex the problem may be, the upper-bound method can be used to obtain an actual value for the failure load, which is very practical for engineers. This method is based on the principle of virtual work, which can be expressed as follows:

$$\int_A T_i v_i dA + \int_V F_i v_i dV = \int_V \sigma_{ij} \varepsilon_{ij} dV \tag{21}$$

where v_i = the velocity of failure block, σ_{ij} and ε_{ij} = the internal stress and the corresponding plastic strain rate, respectively, T_i and F_i = the surface force and body force acting on foundations, respectively, A and V = the area and volume of the integration region, respectively.

3.2. Discrete Failure Mechanism

The failure mechanism under a static state is generally symmetrical, and the most common types are the Prandtl mechanism and the multi-block mechanism. The Prandtl mechanism only divides the failure area into three regions with fewer variables and faster calculation speed. Nevertheless, the multi-block mechanism divides the failure area into many blocks, and a smaller bearing capacity value can be obtained by optimizing multiple variables. This article proposes a new discrete failure mechanism based on these two mechanisms, simultaneously meeting the advantages of fast computation speed and small upper solutions. As shown in Figure 3, the transition zone BB_1B_{n+1} in the Prandtl mechanism is discretized into n triangles, each with a top angle $\delta\theta$ and a bottom angle $\pi/2 + \varphi_L$. The active zone ABB_1 is an isosceles triangle with a base angle of α, and the passive zone $B_1B_{n+1}C$ is assumed to have a base angle of β, so there are only three unknown variables (α, β, φ_L) in this new failure mechanism. The sine theorem can be applied to calculate the side length of each triangle:

$$l_{i+1} = l_i \frac{\cos\varphi_L}{\cos(\delta\theta + \varphi_L)} \qquad 1 \le i \le n \tag{22}$$

$$d_i = l_i \frac{\sin\delta\theta}{\cos(\delta\theta + \varphi_L)} \qquad 1 \le i \le n \tag{23}$$

where l_i and d_i are the length of line BB_i and line B_iB_{i+1}, respectively, with $l_1 = B\sec\theta/2$. Furthermore, the length of line BC and line $B_{n+1}C$ can also be calculated as $l_{n+2} = |BC| = l_{n+1}\frac{\cos\varphi_L}{\cos(\beta+\varphi_L)}$ and $d_{n+1} = |B_{n+1}C| = l_{n+1}\frac{\sin\beta}{\cos(\beta+\varphi_L)}$, respectively.

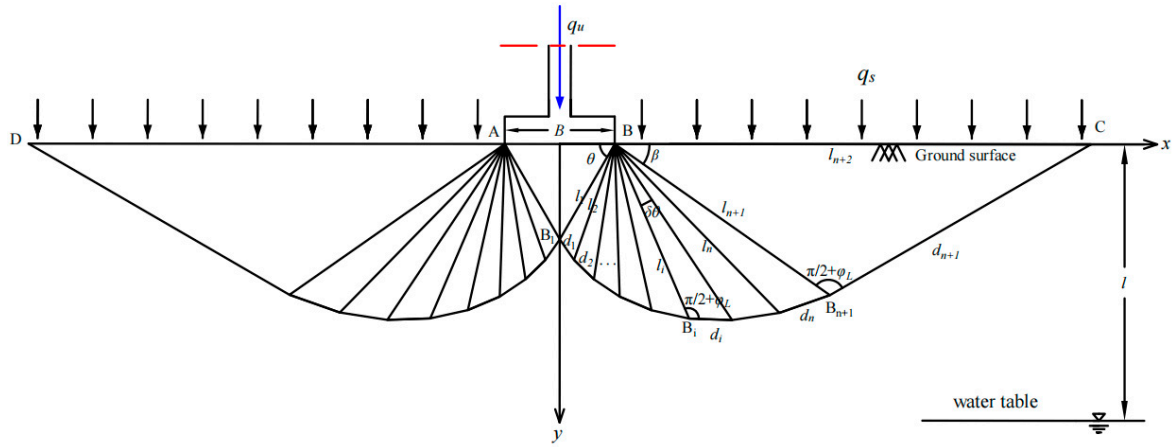

Figure 3. Discrete collapse mechanism for strip footings under unsaturated transient infiltration.

In order to form an admissible velocity field in kinematics, each triangular block slides to one side of the surface, and its velocity v_i forms an angle of φ' with the line d_i. Moreover, the relative velocity $[v]_i$ direction of adjacent triangles also has an angle of φ' with the shared line l_i. The velocity field is shown in Figure 4. Because of the symmetry in the mechanism, only half of its velocity field needs to be studied. Assuming the isosceles triangle ABB_1 moves vertically downwards at the speed of v_0, the velocity field can be calculated as:

$$v_i = \begin{cases} \frac{\cos(\theta-\varphi')}{\cos(\varphi_L-2\varphi')} v_0 & i=1 \\ \frac{\cos(\varphi_L+\delta\theta-2\varphi')}{\cos(\varphi_L-2\varphi')} v_{i-1} & 2 \le i \le n+1 \end{cases} \tag{24}$$

$$[v]_i = \begin{cases} \frac{\sin(\theta+\varphi'-\varphi_L)}{\cos(\varphi_L-2\varphi')} v_0 & i=1 \\ \frac{\sin\delta\theta}{\cos(\varphi_L-2\varphi')} v_{i-1} & 2 \le i \le n+1 \end{cases} \tag{25}$$

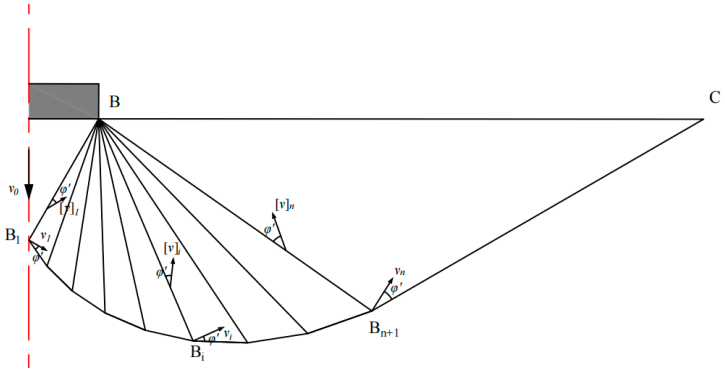

(**a**)

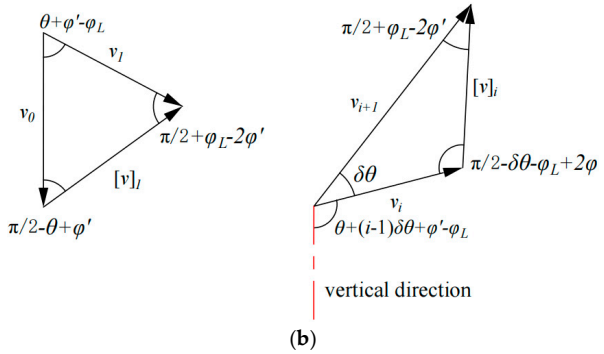

(**b**)

Figure 4. (**a**) Velocity field for the discrete collapse mechanism. (**b**) Velocity hodographs.

3.3. Computation of the Working Rate

Due to the fact that the cohesion of unsaturated soils is composed of effective cohesion c' and apparent cohesion c_{app}, the total internal energy dissipation D_{int} can also be divided into two parts, namely:

$$D_{\text{int}} = D_e + D_a \tag{26}$$

where D_e and D_a are the dissipation caused by effective cohesion c' and apparent cohesion c_{app}, respectively. The effective cohesion c' remains a constant as time and space change, thus:

$$D_c = \sum_{i=1}^{n+1} D'_{\text{OB}_\text{i}} + \sum_{i=1}^{n} D'_{\text{B}_\text{i}\text{B}_\text{i+1}} + D'_{B_{\text{n+1}}\text{C}} = c\cos\varphi' \sum_{i=1}^{n+1} (l_i[v]_i + d_i v_i) \tag{27}$$

However, the apparent cohesion c_{app} caused by one-dimensional transient infiltration varies nonlinearly along the depth, so numerical integration is needed to calculate D_a.

$$\begin{aligned} D_a &= \sum_{i=1}^{n+1} D_{\text{OB}_\text{i}} + \sum_{i=1}^{n} D_{\text{B}_\text{i}\text{B}_\text{i+1}} + D_{\text{B}_{\text{n+1}}\text{C}} \\ &= \sum_{i=1}^{n+1} \int_0^{l_i \sin\theta_i} c_{app}[v]_i \cos\varphi' \tfrac{dy}{\sin\theta_i} - \tfrac{1}{2}\sum_{i=1}^{n} \left[\sigma^s_{B_i} + \sigma^s_{B_{i+1}}\right] d_i v_i \sin\varphi' \\ &+ \int_0^{d_{n+1}\cos(\beta+\varphi_L)} c_{app} v_{n+1} \cos\varphi' \tfrac{dy}{\cos(\beta+\varphi_L)} \end{aligned} \tag{28}$$

where $\sigma^s_{B_i}$ and $\sigma^s_{B_{i+1}}$ represent the suction stress of points B_i and B_{i+1}, respectively. The coordinate system of the failure mechanism takes point O as the origin, with the vertical downward direction being the y-axis positive direction and the horizontal rightward direction being the x-axis positive direction. It is worth noting that the y value for a certain point in the underground soil is its burial depth, which is different from the z value in Equation (5). The relationship between them is $y = l - z$. For a large value of n, the length of B_iB_{i+1} is short enough that its apparent cohesion c_{app} can be seen as linearly changing.

The total power caused by the external force W_{ext} can be obtained by accumulating the power of each part of the external force, i.e.,:

$$W_{\text{ext}} = W_{q_u} + W_{q_s} + W_\gamma \tag{29}$$

where W_{q_u}, W_{q_0}, and W_γ = external forces caused by the vertical load of the superstructure q_u, the surcharge load q_s, and the soil's self-weight within the collapse mechanism, respectively. Their detailed calculation formulas are as follows:

$$W_{q_u} = \frac{1}{2} q_u B v_0 \tag{30}$$

$$W_{q_0} = q_s l_{n+2} v_{n+1} \cos(\theta + n\delta\theta) \tag{31}$$

$$W_\gamma = \frac{1}{2}\gamma \sum_{i=1}^{n+1} l_i d_i v_i \cos\varphi_L \cos[\theta + (i-1)\delta\theta] + \frac{1}{8}\gamma B^2 \tan\theta v_0 \tag{32}$$

3.4. Bearing Capacity and Optimization

By equaling external work power to internal energy power, a functional balance equation can be expressed as:

$$W_{\text{ext}} = D_{\text{int}} \tag{33}$$

Substituting Equations (26)–(32) into Equation (33) the ultimate bearing capacity q_u of shallow strip footings under transient infiltration can be derived as:

$$q_u = \frac{2(D_e + D_a - W_{q_s} - W_\gamma)}{Bv_0} \tag{34}$$

Indeed, this solution of q_u is an upper-bound solution. To measure the impact of unsaturated infiltration on the bearing capacity of shallow strip footings, this paper modified the classic Terzaghi's expression:

$$q_u = \frac{1}{2}\gamma B N_\gamma + q_s N_q + c' N_c + {q_u}^{suction} \tag{35}$$

where N_γ, N_q, and N_c = the bearing capacity parameters related to γ, q_s, and c', respectively, and ${q_u}^{suction}$ = additional bearing capacity due to transient infiltration. It should be noted that the first three terms are not influenced by transient infiltration in unsaturated soils, and the fourth term is also independent of the first three terms' parameters and only related to the matric suction profile. When calculating one of these four items separately, the relevant parameters related to the other items are assumed to be 0. According to Equation (34), the expressions for N_γ, N_q, N_c, and ${q_u}^{suction}$ can be derived as:

$$N_\gamma = -\frac{4W_\gamma}{\gamma B^2 v_0} \tag{36}$$

$$N_q = -\frac{2W_{q_s}}{q_s B v_0} \tag{37}$$

$$N_c = \frac{2D_e}{c' B v_0} \tag{38}$$

$${q_u}^{suction} = \frac{2D_a}{Bv_0} \tag{39}$$

From the derivation process for the upper bound solution above, it can be seen that the bearing capacity is only related to three variables, namely:

$$q_u = f(\theta, \delta\theta, \beta) \tag{40}$$

The smaller the upper bound solution, the more engineering practicality there is. In this paper, the multi-objective sequential quadratic programming (SQP) algorithm is used for optimization, with the detailed process shown in Figure 5 and the constraints listed in Table 1. The current study considers three hypothetical soils: fine sand, silt, and clay, whose typical parameters are recorded in Table 2 [30]. In all data analyses below, it is assumed that the initial infiltration intensity $q_A = 0$, the infiltration intensity variation coefficient $m = 0$, the width of the foundation $B = 1$ m, the surcharge load $q_0 = 10$ kPa, and the unit soil gravity $\gamma = 20$ kN/m^3, if not stated otherwise.

Table 1. Limitations to be embedded in the algorithm.

	Constraints/Conditions
Geometric compatibility	$\theta + n\delta\theta + \beta = \pi$ and $\varphi_L + \beta < \pi/2$
Kinematic admissibility	$v_{i+1} > v_i$ and $v_i > 0$
Range of values	$0 < \theta,\ \delta\theta,\ \beta < \pi/2$

Table 2. Input parameters for the four types of soils used in present study.

Soil Type	α **(m^{-1})**	k_s **(m·s^{-1})**	θ_s	θ_r	c' **(kPa)**	φ'
Fine sand	0.7	5.0×10^{-6}	0.41	0.05	0	30°
Silt	0.5	9.0×10^{-7}	0.45	0.10	5	25°
Clay	0.13	5.0×10^{-8}	0.58	0.05	10	20°

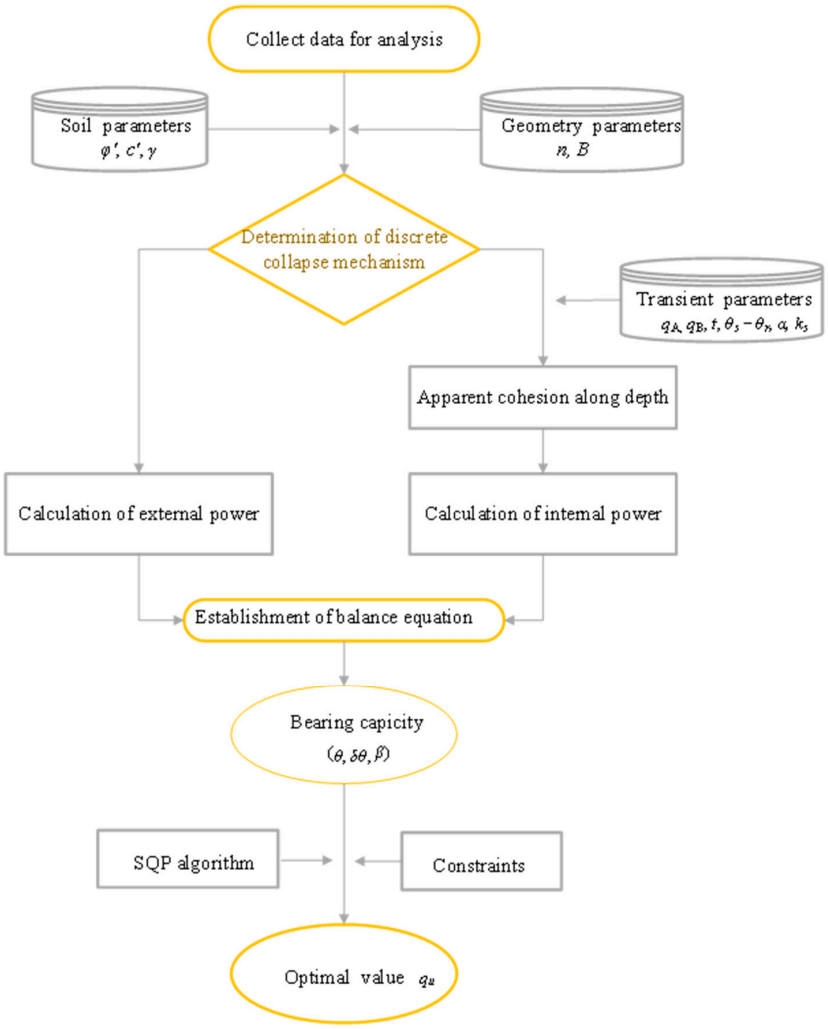

Figure 5. Flowchart for obtaining the optimal upper solution of bearing capacity.

A convergence study is needed to determine the optimal number n of discrete triangles in the passive zone. Apparently, a larger value of n means a more accurate solution, which means a greater computational workload at the same time. So, this convergence study needs to balance these two contradictory requirements. Figure 6 takes sand as an example and obtains its bearing capacity q_u corresponding to different n values according to Equation (34). From Figure 6, it can be seen that as n increases from 5 to 40, q_u continues to increase, whereas the rate of increase gradually slows down. When n increases from 25 to 30, the bearing capacity only increases by 0.19%. Therefore, throughout the entire analysis process, n can be reasonably taken as 30.

This paper provides two methods to calculate the ultimate bearing capacity q_u of strip footings under the action of transient infiltration. Method 1 is an individual method in which the ultimate bearing capacity q_u is calculated by superimposing the contributions of the effective cohesion, the surcharge load, the soil's self-weight, and the apparent cohesion to the bearing capacity. Its detailed procedure is to calculate N_γ, N_q, N_c, and $q_u{}^{suction}$ according to Equations (36)–(39) and then substitute them into Equation (35). Method 2 is a joint method, which applies the Equation (34) to computer q_u directly. Assuming the soil is saturated or dry, Table 3 compares the bearing capacity calculated using these two methods with the results from previous studies in the literature [9,50,51]. As can be seen, the results obtained using method 2 are greater than those obtained used method 1 for all comparisons. Furthermore, the present results obtained using both methods are smaller than the previous results, thanks to the innovative discrete mechanism in this paper.

Considering the unsaturated soil subjected to transient infiltration, Table 4 compares the foundation bearing capacity q_u obtained using these two methods for different types of soils. It can be more intuitively seen that method 1 tends to give more conservative results, but the difference between these two methods does not exceed 6%. Compared to the complex optimization algorithm used in method 2, method 1 can be used to calculate q_u easily by directly querying N_γ, N_q, N_c, and ${q_u}^{suction}$ for different operating modes. Therefore, method 1 is recommended for the practical design of foundations.

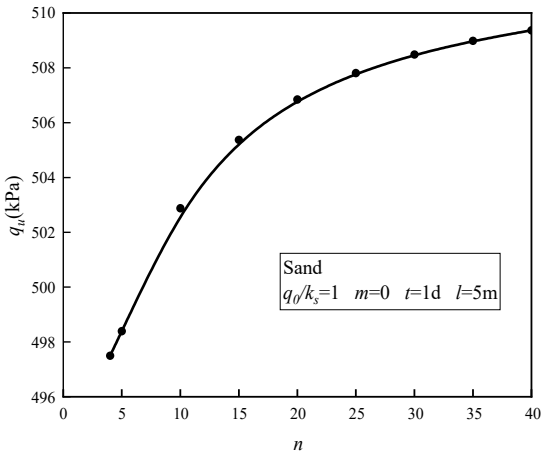

Figure 6. The magnitude of q_{ce} versus different numbers of rigid triangular blocks n.

Table 3. Comparison of bearing capacity with previous studies.

Method	This Study	Soubra [9]	Jin et al. [50]	Wang et al. [51]
Method 1: q_{super} (kN/m^2)	675.18	680.58	686.76	704.89
Method 2: q_u (kN/m^2)	718.30	726.13	728.03	736.19

Note: $\gamma = 18$ kN/m^3, $\varphi' = 30°$, and $c' = 10$ kPa, $q_s = 10$ kPa.

Table 4. Comparison of bearing capacity using the two methods proposed in this study.

φ	Fine sand (t = 1 d)			Silt (t = 4 d)			Clay (t = 60 d)		
	Method 1	Method 2	Difference	Method 1	Method 2	Difference	Method 1	Method 2	Difference
	q_{super}(kN/m^2)	q_u(kN/m^2)	(%)	q_{super}(kN/m^2)	q_u(kN/m^2)	(%)	q_{super}(kN/m^2)	q_u(kN/m^2)	(%)
15	76.81	79.11	2.91	138.21	142.16	2.78	219.95	225.10	2.29
20	136.37	143.12	4.71	222.35	233.16	4.64	345.48	359.07	3.79
25	248.64	265.40	5.92	373.14	396.61	5.92	563.62	592.79	4.92
30	477.84	508.49	5.86	665.66	707.91	5.97	970.85	1025.20	5.30
35	968.38	1027.25	5.73	1266.86	1347.00	5.95	1777.81	1886.00	5.74
40	2118.27	2241.96	5.52	2625.71	2791.37	5.93	3301.02	3367.01	1.96

Note: $l = 5$ m.

4. Verification

Considering that no scholars have yet studied the impact of transient infiltration on the upper-bound solution of the foundation bearing capacity, the validation in this study mainly consists of two steps. Firstly, the feasibility and accuracy of the proposed framework in obtaining the foundation bearing capacity in saturated or dry soil are tested using published research. Then, the correctness of the analytical solution for unsaturated transient infiltration is verified. The apparent cohesion generated by transient infiltration is added to the functional equation as a separate internal energy dissipation term, so as long as these two verification steps are successful, the present method for computing bearing capacity is effective.

4.1. Verification of the Bearing Capacity under the No-Suction Condition

Assuming the strip footing is located on a dry or saturated soil layer, its N_γ, N_c, and N_q values obtained using method 1 are compared with previous results [8–10,51–53], as listed in Tables 5–7. It is worth noting that the theory used by Vesic [52] and Zhu [10] is the limit

equilibrium theory, while all other solutions are upper-bound solutions. For the values of N_γ recorded in Table 5, the present results gradually become the least upper-bound solutions as the φ value increases, while Chen's results are the largest from beginning to end. The difference in the N_γ value is mainly caused by the variety of collapse mechanisms. Chen [53] applied the symmetric Prandtl mechanism, whereas Michalowski [8], Soubra [9], and Zhu [10] applied the multi-block mechanism, whose periphery does not assume any shape. Apparently, the bearing capacity solutions for the multi-block mechanism are all smaller than those for the Prandtl mechanism. Moreover, both Soubra [9] and Zhu [10] observed that the average reduction in upper-bound solutions calculated using the symmetric mechanism was 23.12% compared with those obtained using the unilateral mechanism. Similarly, the limit equilibrium solutions achieved using the symmetric mechanism were found to be, on average, 2.85% smaller than those attained using the unilateral mechanism. Therefore, the symmetrical mechanism is more suitable for the calculation of bearing capacity under a static state.

Table 5. Comparison of N_γ with previous studies.

$\varphi(^\circ)$	This Study	Wang et al. [51]	Soubra [9]		Michalowski [8]	Chen [53]	Zhu [10]	
	Symmetrical	One-Sided	Symmetrical	One-Sided	Symmetrical	Symmetrical	Symmetrical	One-Sided
15	2.49	3.53	1.95	2.10	1.94	2.94	1.94	2.10
20	4.89	6.56	4.49	4.67	4.47	6.20	4.47	4.66
25	9.89	12.26	9.81	10.06	9.77	12.96	9.76	10.03
30	21.42	24.21	21.51	21.88	21.39	27.67	21.38	21.81
35	48.36	50.94	49.00	49.62	48.68	61.47	48.65	49.38
40	117.17	122.95	119.84	120.96	118.83	145.19	118.76	120.15
45	315.98	331.22	326.59	328.88	322.84	374.02	322.62	325.77

Table 6. Comparison of N_c with previous studies.

$\varphi(^\circ)$	This Study	Wang et al. [51]	Soubra [9]		Vesic [52]
	Symmetrical	One-Sided	Symmetrical	One-Sided	Symmetrical
15	10.94	11.38	10.99	11.00	10.98
20	14.75	15.00	14.86	14.87	14.83
25	20.56	20.80	20.77	20.78	20.72
30	29.83	30.20	30.24	30.25	30.14
35	45.52	46.50	46.33	46.35	46.12
40	74.07	75.90	75.77	75.80	75.12
45	131.12	141.38	134.99	135.09	133.88

From Tables 6 and 7, it is easy to see that for all φ values, the present values of both N_c and N_q are the smallest. The results of Wang et al. [51] are the largest, followed by Soubra [9]. This is because Wang et al. [51] used the multi-wedge discrete mechanism, whose wedge includes quadrilaterals. In contrast, the discrete blocks in this paper and those used by Soubra [9] contain only triangles, which are more advantageous. Overall, assuming that discrete blocks have the same top and bottom angles, the multi-block mechanism proposed in this study avoids the computational complexity caused by too many variables. At the same time, it also provides a good basis for numerical integration of apparent cohesion.

Table 7. Comparison of N_q with previous studies.

$\varphi(^\circ)$	This Study	Wang et al. [51]	Soubra [9]		Vesic [52]
	Symmetrical	One-Sided	Symmetrical	One-Sided	Symmetrical
15	3.94	3.94	3.95	3.95	3.94
20	6.40	6.47	6.41	6.41	6.40
25	10.67	10.72	10.69	10.69	10.66
30	18.41	18.50	18.46	18.46	18.40
35	33.30	33.31	33.44	33.43	33.30
40	64.26	64.90	64.58	64.55	64.20
45	134.53	141.38	135.99	135.91	134.87

4.2. Verification of the Matric Suction Profile with Infiltration Time

The finite element analysis software *Geo-Studio* is applied to verify the correctness of the analytical solution for transient infiltration in unsaturated soils. As shown in Figure 7,

a rectangular soil layer with a length of 5 m and a height of 3 m is first established. It is assumed that the buried depth of the water table is 3 m, and the soil is fine sand. A total of 172.8 mm of rain falls on the foundation for 24 h. Prior to this rainfall, the area where the foundation is located had not experienced rainfall for a long time, so $q_A = 0$. The seepage analysis module *SEEP/W* is used to apply a boundary condition of late infiltration intensity q_B at the surface. To ensure that rainfall is the same, three scenarios for linear changing rainfall intensity are set: (1) scenario 1 (advanced-peak infiltration): q_B decreases from 3×10^{-6} m/s to 1×10^{-6} m/s, which means $q_0 = 3 \times 10^{-6}$ m/s and $m = -2.315 \times 10^{-11}$ m/s^2; (2) scenario 2 (uniform infiltration): $q_B = 2 \times 10^{-6}$ m/s remains unchanged, which means $q_0 = 2 \times 10^{-6}$ m/s and $m = 0$; and (3) scenario 3 (delayed-peak infiltration): q_B increases from 1×10^{-6} m/s to 3×10^{-6} m/s, which means $q_0 = 1 \times 10^{-6}$ m/s and $m = 2.315 \times 10^{-11}$ m/s^2.

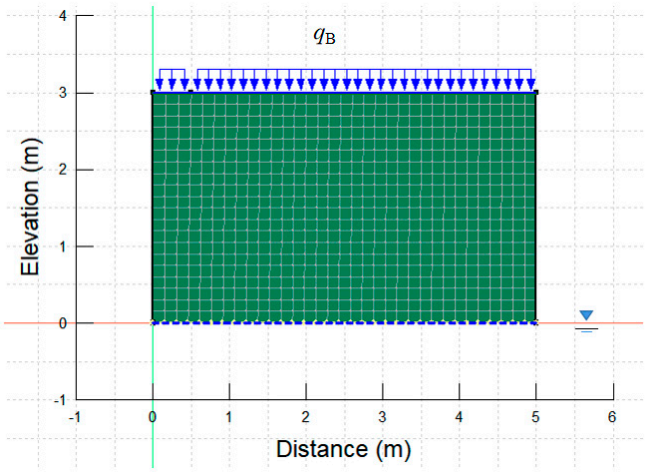

Figure 7. Finite element model for a foundation under rainfall infiltration.

For the matric suction profile of these three scenarios, Figure 8 compares the numerical solutions using the software *Geo-Studio* with the analytical solutions calculated according to Equations (12) and (18). It can be easily observed that no matter the type of rainfall, the magnitude and variation in matric suction obtained using the two methods are almost the same, indicating that the analytical expression for transient seepage derived in this paper is correct. In addition, the soil matric suction along the depth changes from linear to nonlinear during rainfall. As time goes on, the magnitude of matric suction in the middle and upper part of the foundation is decreasing, and the decreasing amplitude and the affected area's depth are increasing. Comparing these three different rainfall types, when t = 0, the distribution of matric suction is identical. When t = 6 h, the magnitude of matrix suction at all depths is ranked as advanced-peak infiltration < uniform infiltration < delayed-pack infiltration. The reason for the largest reduction in matric suction in advanced-peak infiltration lies in its maximum rainfall amount at t = 6 h. However, over time, the differences in matric suction between the three types gradually decrease, as their rainfall amounts converge toward the same. Finally, a stress analysis module *SIGMA/W* is superimposed based on the seepage field of t = 24 h. The load of the foundation is applied as a function of the displacement boundary condition. Note that the left side of the model is the symmetry axis of the middle line, so the actual foundation width is 1 m. Figure 9 presents a velocity vector diagram for each point in the soil layer during the foundation failure. It is seen that the failure envelope in Figure 9 is highly similar to that of the present discrete failure mechanism in Figure 3.

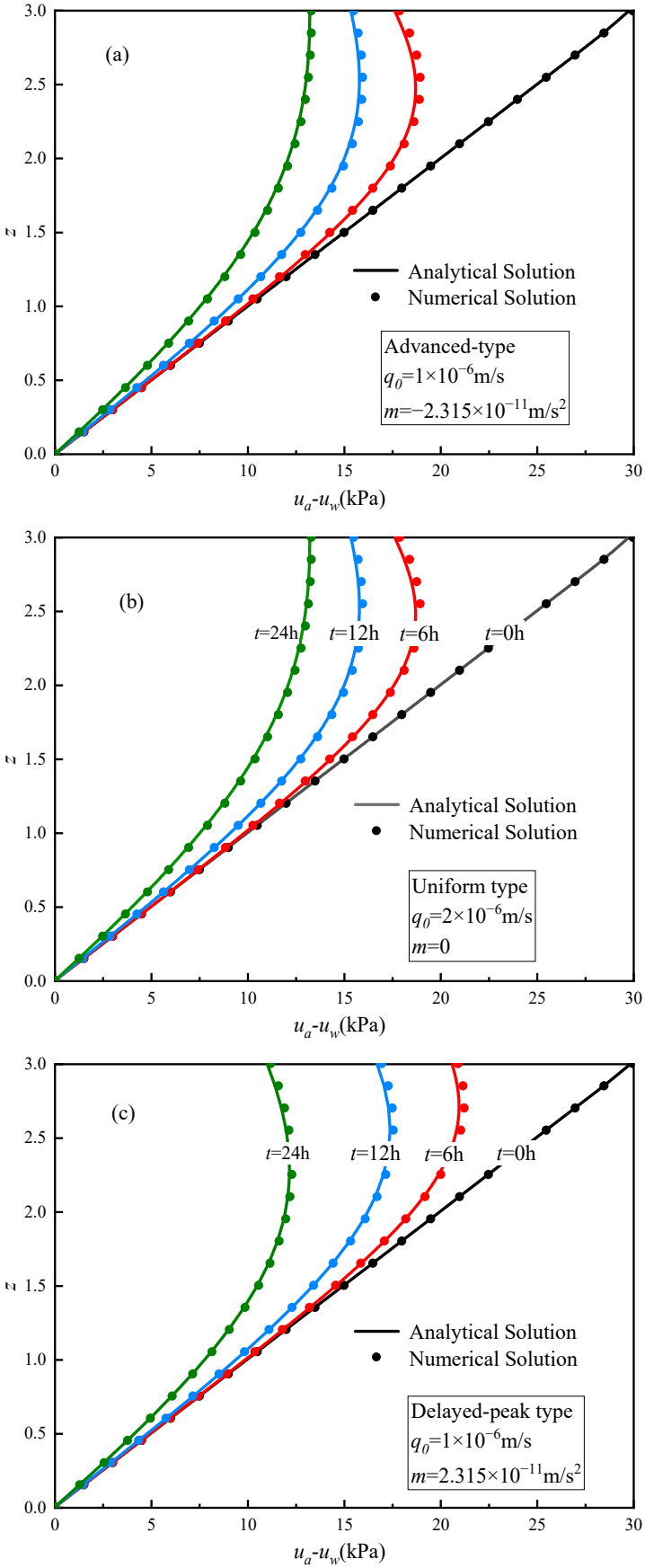

Figure 8. Distribution of matric suction along depth under (**a**) advanced-peak infiltration, (**b**) uniform infiltration, and (**c**) delayed-peak infiltration.

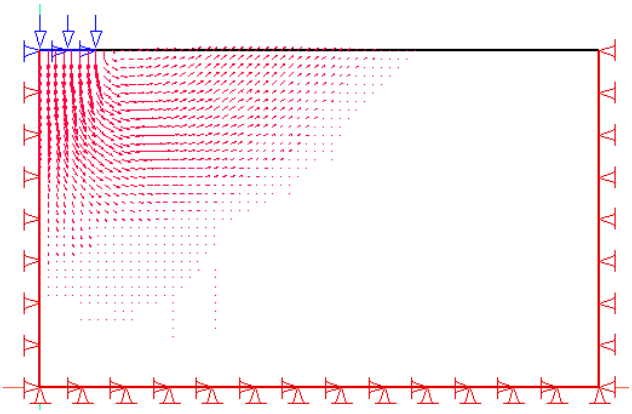

Figure 9. Soil velocity vector diagram during foundation failure.

5. Results and Discussion

5.1. Saturation Degree and Apparent Cohesion Profiles

To explore the response of unsaturated soil under transient seepage, Figures 10–12 describe the saturation degree S_e and apparent cohesion c_{app} distributions of fine sand, silt, and clay at different times t and with different water table depths l. It is assumed that $q_0/k_s = 1$ and $m = 0$. Obviously, the development of transient flow is affected by soil type, water table depth, infiltration time, and distance from the study site to the ground. From Figures 10a, 11a and 12a, as the infiltration time t increases, the saturation degree S_e of all soils increases, eventually converging to 1.0 at all depths. These three soils reach complete saturation at different times. Specifically, infiltration of fine sand is a rapid process, often reaching full saturation in less than 10 days, while infiltration of silt is much slower, usually taking tens of days, and clay is the slowest, taking hundreds of days. The water table depth l also affects the process of soil saturation under the action of transient flow. It can be seen that when the water table depth is increased from 3 m to 6 m, the time required to reach the full saturation state is almost doubled. And the deeper the water table, the greater the saturation degree S_e of the soil at the same depth at the same time. Furthermore, as time progresses, the soil near the surface experiences a higher increase in saturation degree S_e compared to the middle soil. As a result, the upper and lower parts of the soil layer exhibit a higher saturation degree S_e, while the middle part remains relatively low in saturation degree S_e.

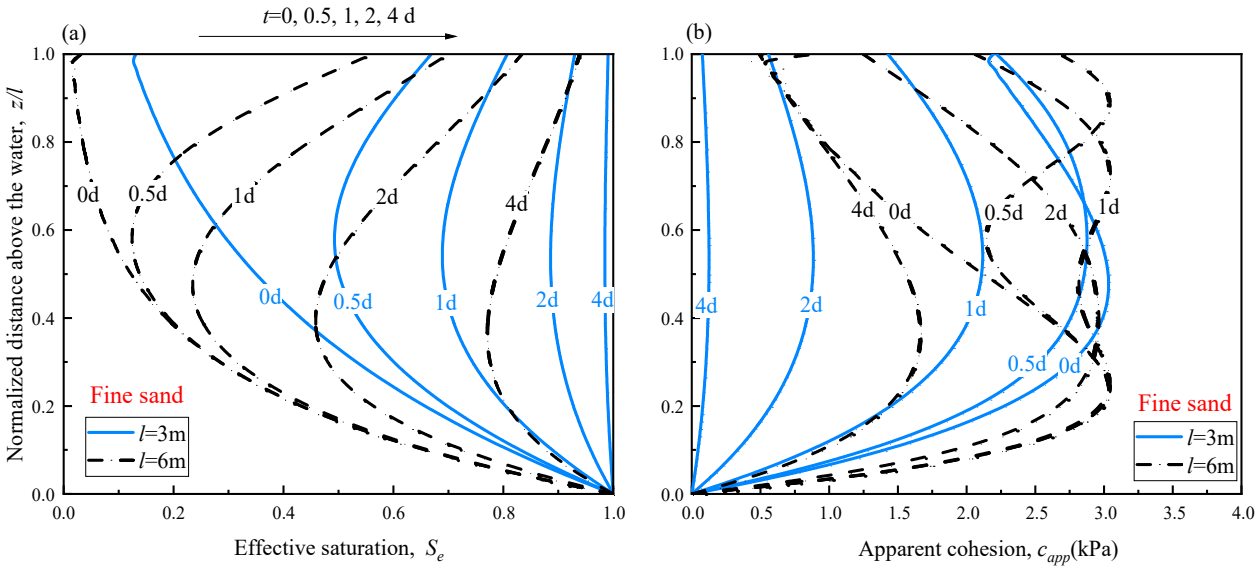

Figure 10. Profiles of (**a**) effective saturation S_e and (**b**) apparent cohesion c_{app} for fine sand.

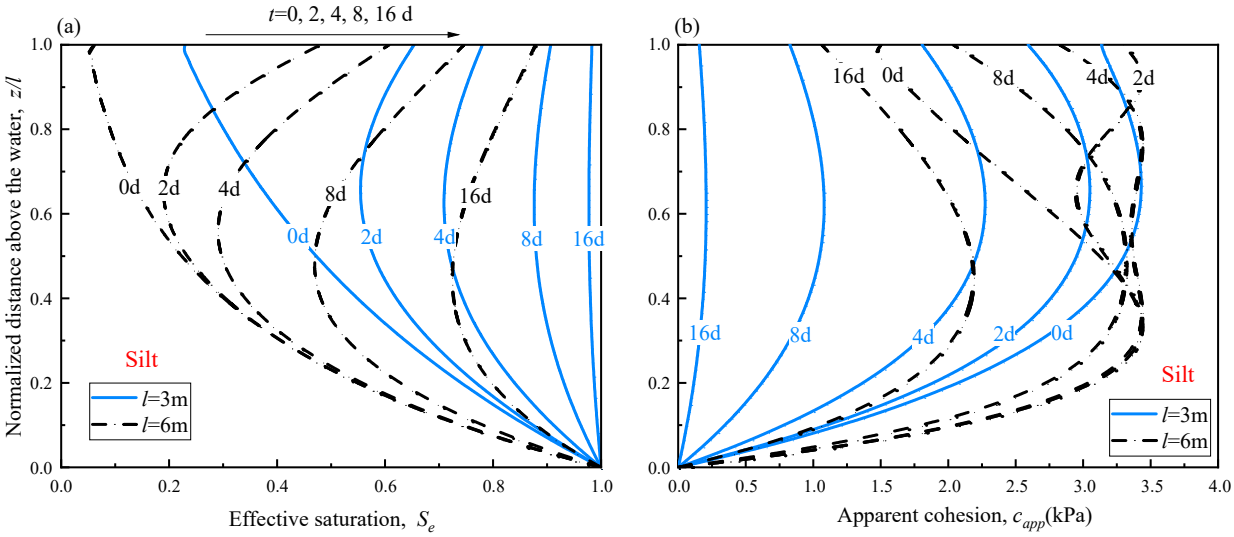

Figure 11. Profiles of (**a**) effective saturation S_e and (**b**) apparent cohesion c_{app} for silt.

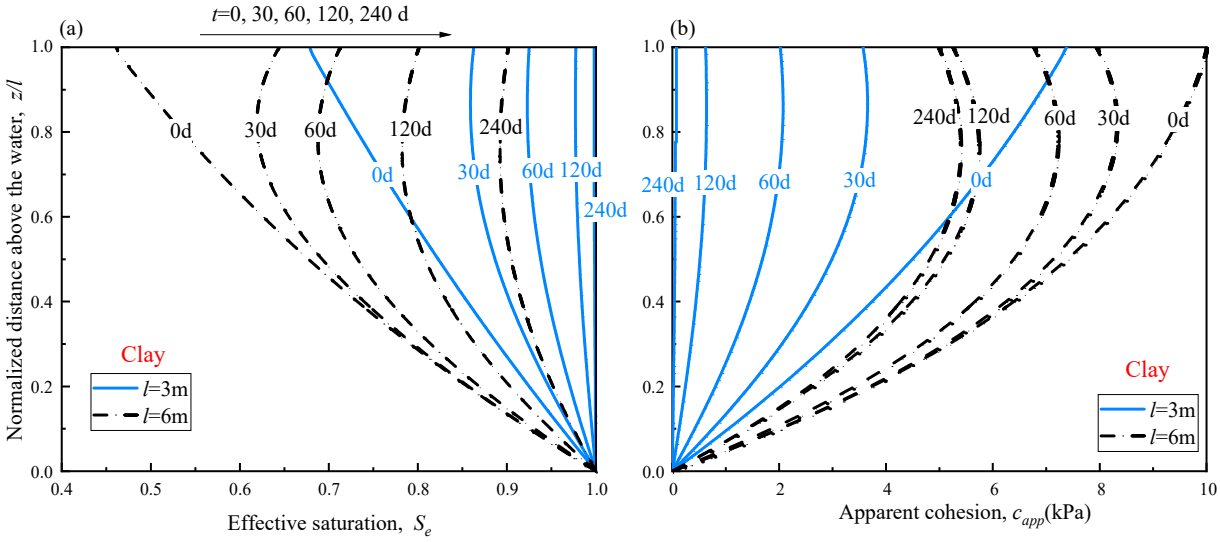

Figure 12. Profiles of (**a**) effective saturation S_e and (**b**) apparent cohesion c_{app} for clay.

The complexity of apparent cohesion variation is undeniable, yet there are still fundamental rules that govern it. From Figures 10b, 11b and 12b, the apparent cohesion c_{app} of the three soils will eventually converge to 0 as time goes by. Notably, the convergence time to zero cohesion aligns closely with the time required for complete soil saturation. This is actually because there is no apparent cohesion in fully saturated soil, which reaffirms the validity of the findings presented in this study. For clay, regardless of whether the water table depth is 3 m or 6 m, its apparent cohesion c_{app} generally decreases over time. Moreover, the trend in c_{app} along the depth is similar to that of S_e. When the water table drops from 3 m to 6 m, the clay's c_{app} at the same depth and time double. However, for fine sand and silt, when the water table is shallow (l = 3 m), their apparent cohesions c_{app} initially increase and then decrease with increasing depth. However, when the water table drops to 6 m, the profile of c_{app} becomes disordered. These differences in cohesion variations among different soils are primarily attributed to variations in the values of α and k_s, which result in different saturation degrees S_e.

The apparent cohesion c_{app} can be obtained by substituting the saturation into Equation (20). Differentiating Equation (20) with respect to K yields:

$$\frac{dc_{app}}{dK} = -\frac{\gamma_w}{\alpha}\tan\varphi'(\ln K + 1) \tag{41}$$

When the saturation exceeds 1/e, the apparent cohesion c_{app} decreases as the saturation degree S_e. increases. Conversely, when c_{app} is less than 1/e, the opposite trend occurs, as shown in Figure 13. Therefore, the maximum value of c_{app} occurs when S_e equals 1/e, which is consistent with the trend depicted in Figures 10–12.

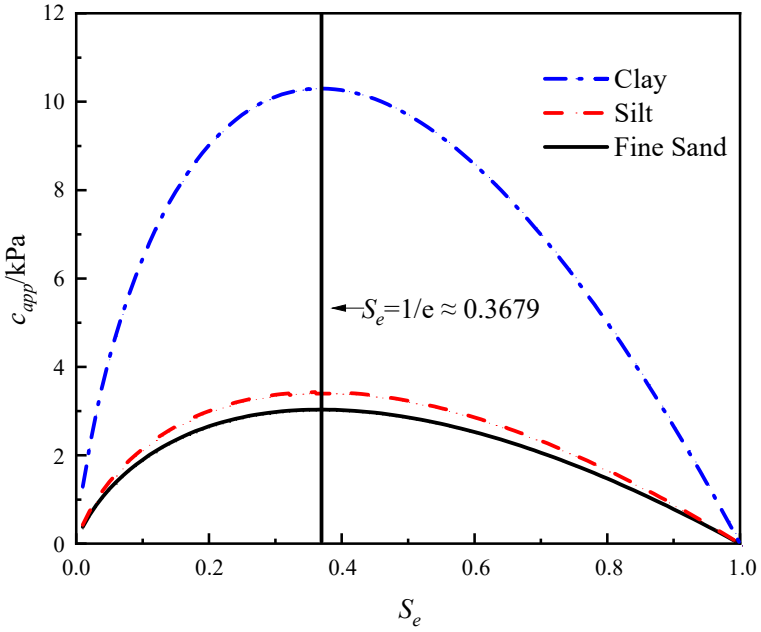

Figure 13. Apparent cohesion versus S_e for different types of soils.

5.2. Parametric Analysis

The previous discussion demonstrated that the additional bearing capacity ${q_u}^{suction}$ caused by transient seepage is an independent item, unrelated to the effective cohesion c', surcharge load q_s, and unit weight of soil γ. The dimensionless bearing capacity factors N_γ, N_q, and N_c, which are recorded in Tables 5–7, are only related to the effective internal friction angle φ'. Therefore, the parametric analysis in this section is specifically focused on the additional bearing capacity ${q_u}^{suction}$. By analyzing Equation (39), it can be determined that the parameters influencing ${q_u}^{suction}$ are the permeability coefficient (k_s), infiltration intensity (q_B), water storage capacity ($\theta_s - \theta_r$), effective internal friction angle (φ'), desaturation coefficient (α), rainfall duration (t), and water table depth (l). For the purpose of simplification, the analysis assumes uniform rainfall for transient infiltration, i.e., $q_B = q_0$.

Figures 14–16 depict the results of the additional bearing capacity ${q_u}^{suction}$ for the three soil types, involving different infiltration times t, water table depths l, and infiltration ratios q_0/k_s. From the graphs, it can be observed that at t = 0, the value of ${q_u}^{suction}$ due to matric suction in unsaturated soils does not vary with changes in q_0/k_s. Among these three soil types, clay exhibits the highest value of ${q_u}^{suction}$, followed by silt, and then fine sand. For example, when t = 0 days and l = 6 m, the bearing capacity of the foundation increases by 23.60 kPa for fine sand, 36.07 kPa for silt, and 143.80 kPa for clay. Furthermore, as the water table depth increases from 4 m to 8 m, the initial response of ${q_u}^{suction}$ differs for different soil types. Fine sand and silt present an increasing trend, with the values decreasing from 59.04 kPa to 7.96 kPa and from 61.01 kPa to 18.26 kPa, respectively. However, clay consistently increases from 115.73 kPa to 152.52 kPa. With the development of transient seepage, the influence of water table variations in ${q_u}^{suction}$ becomes disordered for fine sand and silt. However, the value of ${q_u}^{suction}$ for clay continues to increase as the water table drops, aligning with the trend in the apparent cohesion variation observed in Figures 10–12.

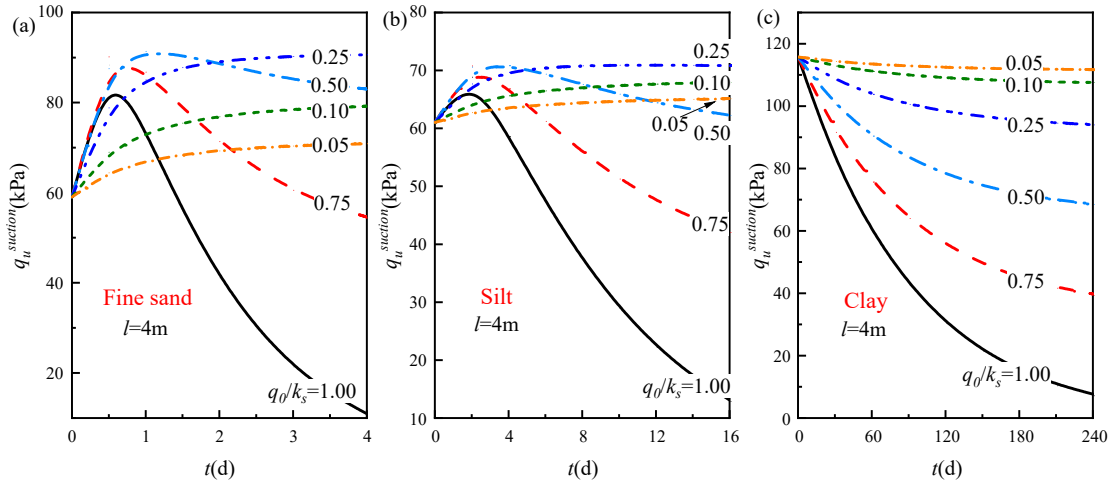

Figure 14. Additional bearing capacity $q_u{}^{suction}$ versus infiltration time t for l = 5 m in (**a**) fine sand, (**b**) silt, and (**c**) clay.

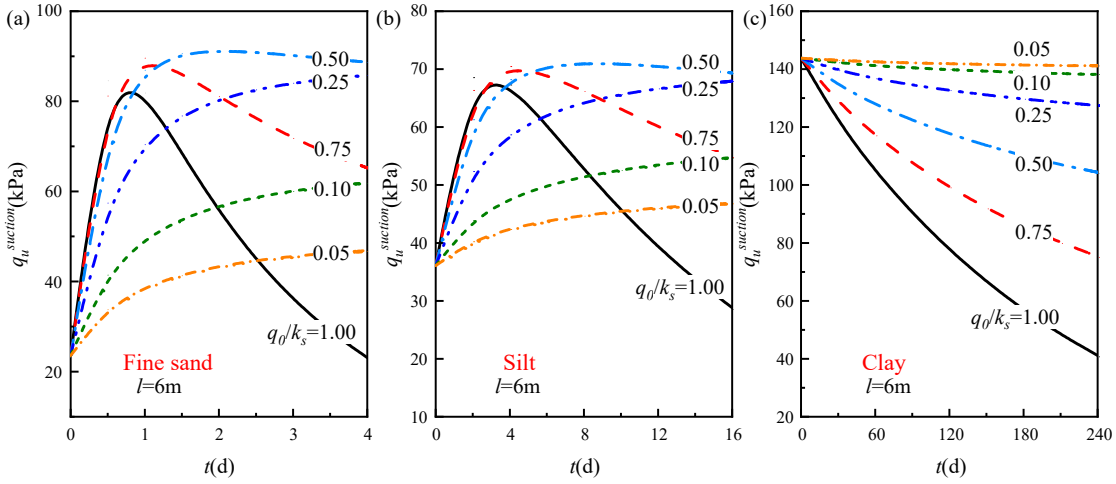

Figure 15. Additional bearing capacity $q_u{}^{suction}$ versus infiltration time t for l = 6 m in (**a**) fine sand, (**b**) silt, and (**c**) clay.

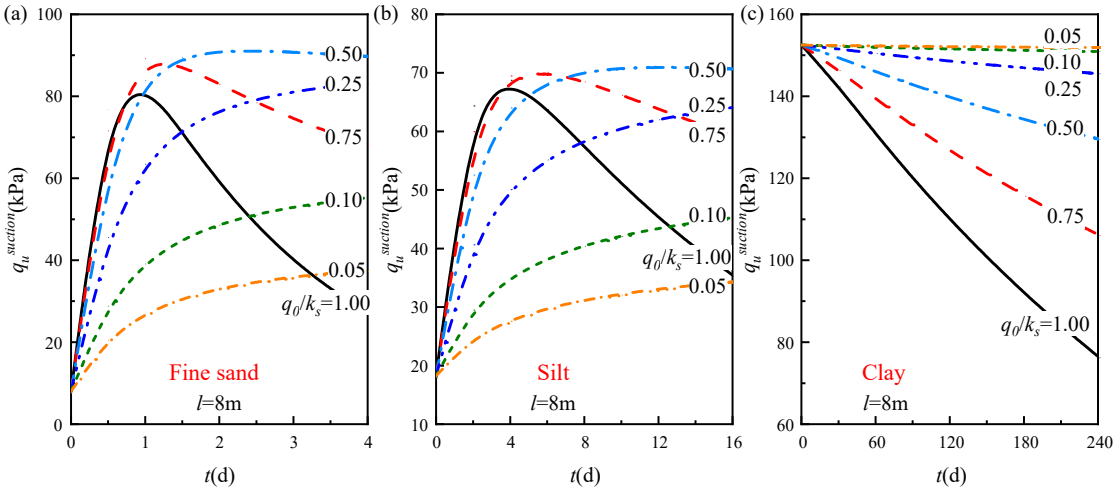

Figure 16. Additional bearing capacity $q_u{}^{suction}$ versus infiltration time t for l = 8 m in (**a**) fine sand, (**b**) silt, and (**c**) clay.

It is important to pay attention to the influence of the infiltration ratio q_0/k_s on the additional bearing capacity ${q_u}^{suction}$ of the three soils. Theoretically, the rainfall flux rate is always less than or equal to the saturated hydraulic conductivity of the soil, i.e., $q_0/k_s \leq 1$. Previous studies [2,30,31] have typically assumed that $q_0/k_s = 1$ to simplify the analysis. In practical engineering, due to uncertainties in rainfall and surface water, the infiltration ratio q_0/k_s can take any value between 0 and 1. Therefore, this study considers six scenarios by extending the investigation to different infiltration ratios of q_0/k_s = 0.05, 0.25, 0.10, 0.50, 0.75, and 1. From Figures 14–16, it can be observed that for a given water table depth and infiltration ratio q_0/k_s, the ${q_u}^{suction}$ for fine sand and silt show a similar trend over time, while the ${q_u}^{suction}$ for clay monotonically decreases over time. Specifically, for fine sand and silt, when $q_0/k_s \geq 0.50$, their ${q_u}^{suction}$ value initially increases and then decreases as time goes by. Moreover, smaller values of q_0/k_s result in larger maximum values of ${q_u}^{suction}$ and longer corresponding infiltration times t. The maximum value of ${q_u}^{suction}$ at $q_0/k_s = 0.50$ is the highest among all scenarios, with magnitudes of 91.15 kPa and 70.44 kPa, respectively. The maximum values of ${q_u}^{suction}$ for fine sand typically occur between 0.5 days and 1 day, while for silt, they occur between 2 days and 4 days. Additionally, in the descending part of the additional bearing capacity over time, a smaller q_0/k_s generates a slower rate of decrease. When $q_0/k_s = 0.05,\ 0.25,\ 0.10$, the ${q_u}^{suction}$ of fine sand and silt monotonically increase with time, but the rate of increase gradually slows down. Furthermore, a larger q_0/k_s leads to a greater magnitude of increase in ${q_u}^{suction}$. The response of clay's ${q_u}^{suction}$ to the development of transient seepage is completely different. As time goes by, the ${q_u}^{suction}$ corresponding to all values of q_0/k_s decreases, and the range of reduction increases with an increase in q_0/k_s.

The reason for the different trends corresponding to different infiltration ratios q_0/k_s is that smaller rainfall flux rates continuously increase the saturation degree of fine sand and silt, but it takes a longer time to reach the inflection point of 1/e, resulting in an increasing trend. However, when the rainfall intensity is larger, the saturation degree quickly reaches 1/e and continues to increase, leading to an initial increase and subsequent decrease in apparent cohesion c_{app}. On the other hand, clay has a saturation degree greater than 1/e initially, so its apparent cohesion c_{app} will decrease regardless of the infiltration flux.

Assuming $q_0/k_s = 0.5$ and $k_s = 5 \times 10^{-6}$, Figures 17–19 depict the variation in additional bearing capacity ${q_u}^{suction}$ with respect to the effective internal friction angle φ' for different values of the water table depth l, water storage capacity $\theta_s - \theta_r$, and desaturation coefficient α. As the water table decreases, ${q_u}^{suction}$ slightly increases. For smaller values of α, an increase in $\theta_s - \theta_r$ also leads to an increase in ${q_u}^{suction}$, although the effect is minor. Clearly, the effective internal friction angle φ' and desaturation coefficient α have more significant impacts on the additional bearing capacity. With an increase in φ', the ${q_u}^{suction}$ continuously increases, and the speed of the increase accelerates. The influence of φ' on ${q_u}^{suction}$ becomes more evident for smaller values of α. For example, when $\theta_s - \theta_r = 0.5$, $\alpha = 0.2$, and l = 8 m, the value of ${q_u}^{suction}$ increases from 27.05 kPa to 1161.52 kPa with increasing φ' from 10° to 40°. From the equation $c_{app} = -\sigma^s \tan \varphi'$, it can be determined that an increase in φ' can directly increase the c_{app}, thereby enhancing ${q_u}^{suction}$. Additionally, as one of the most important parameters of soil, the value of φ' plays a critical role not only in bearing capacity neglecting suction stress but also in seismic bearing capacity [54]. Equations (6) and (7) indicate that the soil water characteristic curve and hydraulic conductivity are both influenced by α. This explains the high sensitivity of additional bearing capacity ${q_u}^{suction}$ to the desaturation coefficient α.

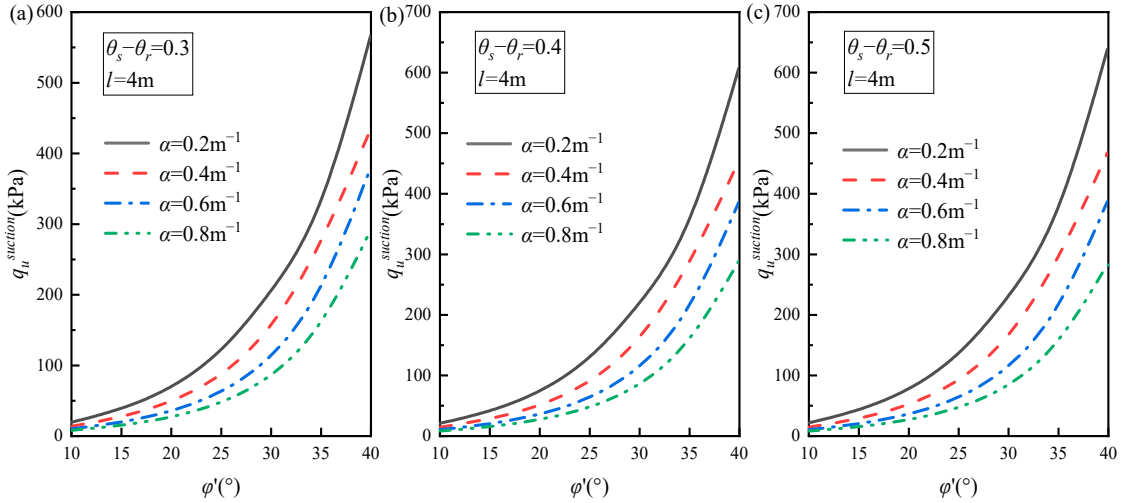

Figure 17. Additional bearing capacity $q_u{}^{suction}$ versus φ' for different values of α for l = 4 m: (**a**) $\theta_s - \theta_r = 0.3$, (**b**) $\theta_s - \theta_r = 0.4$, and (**c**) $\theta_s - \theta_r = 0.5$.

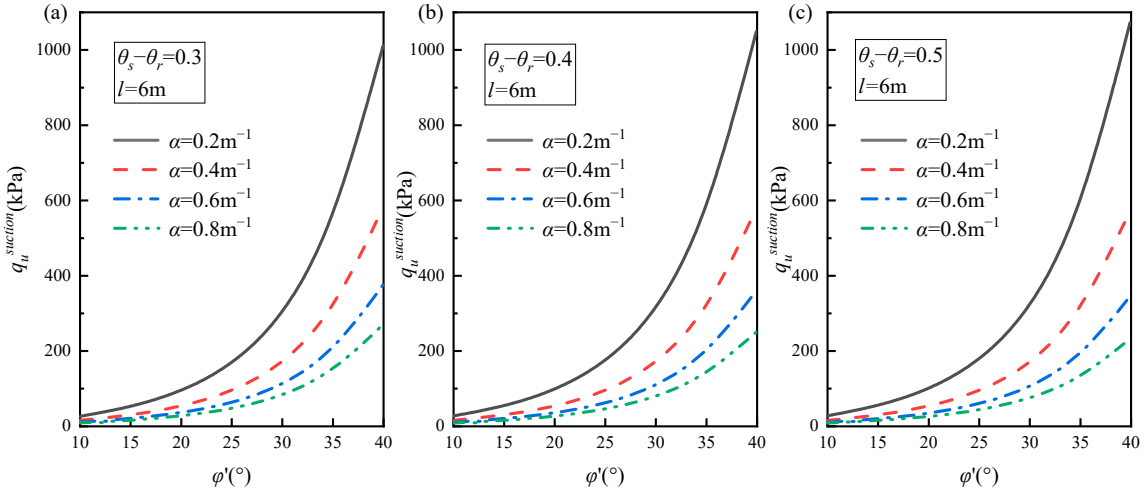

Figure 18. Additional bearing capacity $q_u{}^{suction}$ versus φ' for different values of α for l = 6 m: (**a**) $\theta_s - \theta_r = 0.3$, (**b**) $\theta_s - \theta_r = 0.4$, and (**c**) $\theta_s - \theta_r = 0.5$.

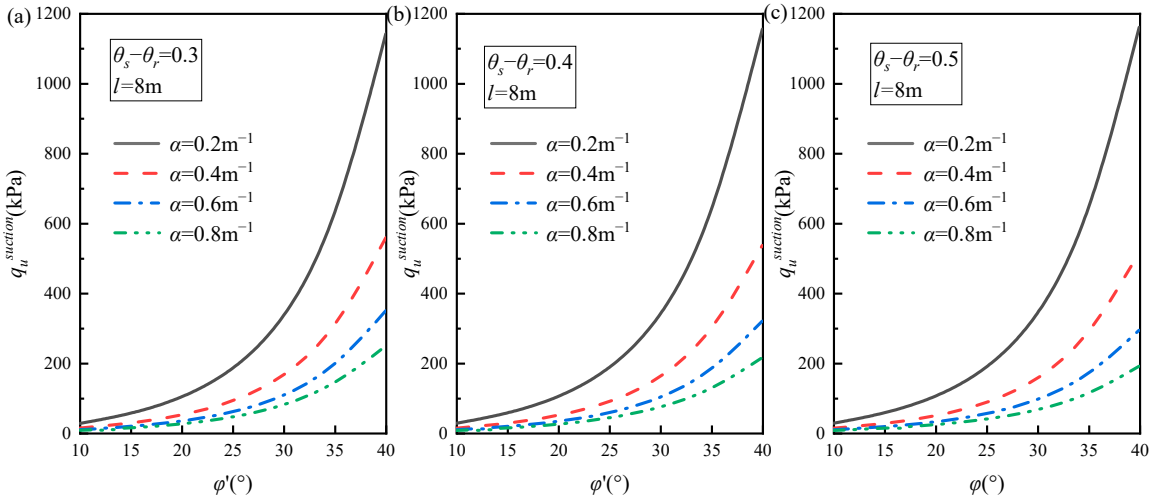

Figure 19. Additional bearing capacity $q_u{}^{suction}$ versus φ' for different values of α for l = 8 m: (**a**) $\theta_s - \theta_r = 0.3$, (**b**) $\theta_s - \theta_r = 0.4$, and (**c**) $\theta_s - \theta_r = 0.5$.

5.3. Collapse Mechanism and Design Tables

The outer contours of the proposed discrete failure mechanisms generated for three kinds of soils with different infiltration times at three different water table depths (l = 4 m, 6 m, and 8 m) are presented in Figure 20. Without considering suction stress, there is no doubt that the bearing capacity of these three kinds of soil is ordered as clay > silt > fine sand. The same is true for the collapse range ordering shown in Figure 20. In fact, considering the effect of transient seepage, the three kinds of soils remain unchanged when l = 4 m and 6 m in order of bearing capacity, as shown in Figure 20. When the water level drops to 8 m, the bearing capacity of fine sand surpasses that of silt, but it is still smaller than that of clay. Furthermore, it can be observed that the water table depth significantly affects the bearing capacity while exerting minimal influence on the collapse range.

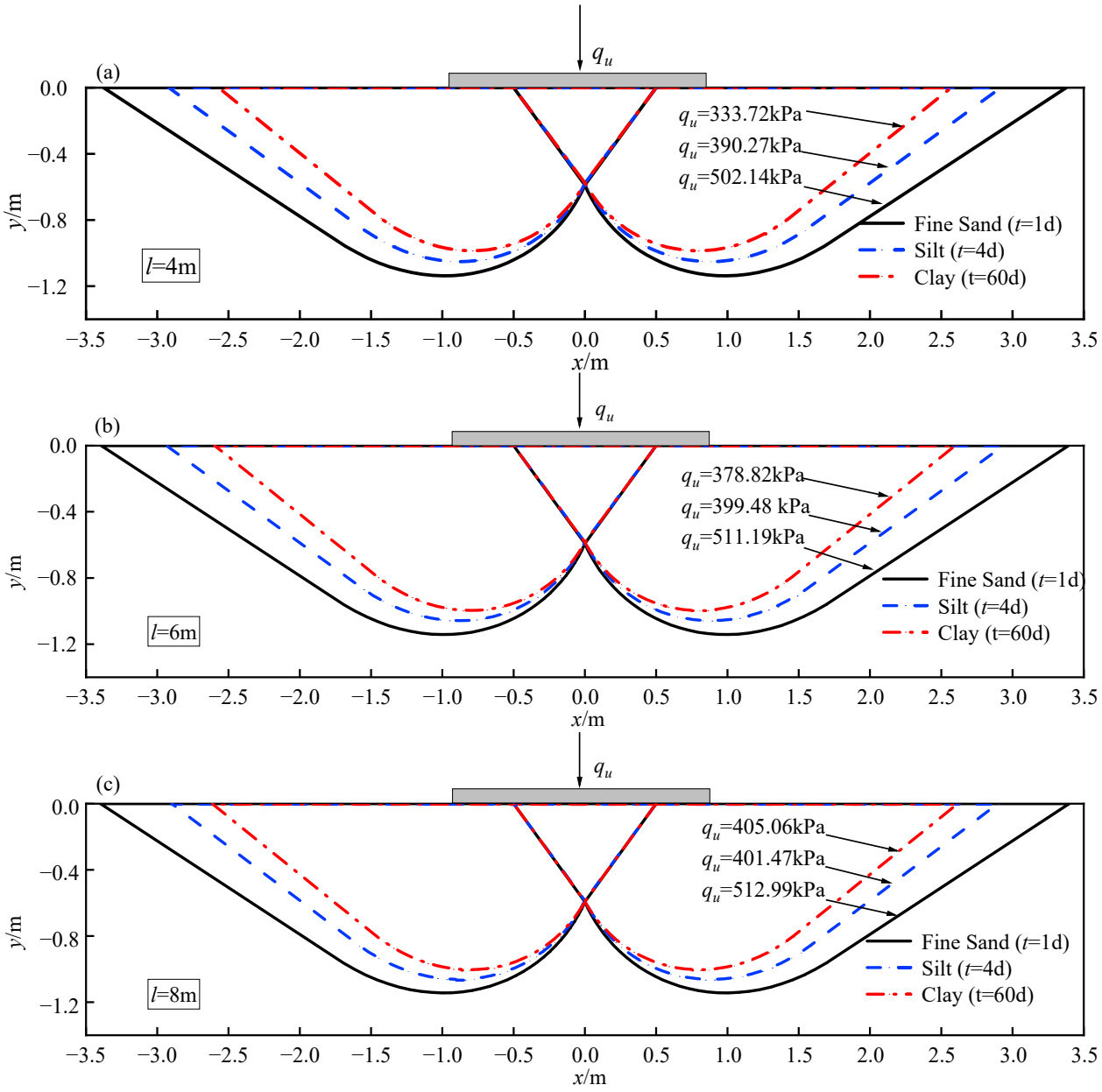

Figure 20. The critical slip surface of the three soils for (**a**) l = 4 m, (**b**) l = 6 m, and (**c**) l = 8 m.

Since the contribution of transient infiltration is a separate part of the ultimate bearing capacity q_u, Tables 8–10 record the addition bearing capacity $q_u{}^{suction}$ for various combinations of φ', t, l, and k_s with the infiltration ratio q_0/k_s being equal to 1.00, 0.75, and

0.50. Applying method 1, these ${q_u}^{suction}$ values can be substituted with N_γ, N_q, and N_c in Tables 5–7 into Equation (35) to calculate the ultimate bearing capacity q_u.

Table 8. Additional bearing capacity ${q_u}^{suction}$ due to transient infiltration ($q_0/k_s = 1$).

$\varphi'(^\circ)$	I(m)	k_s=5×10^{-6}					k_s=5×10^{-7}				k_s=5×10^{-8}			
		t = 0 d	t = 0.5 d	t = 1 d	t = 2 d	t = 4 d	t = 4 d	t = 8 d	t = 12 d	t = 16 d	t = 60 d	t = 120 d	t = 180 d	t = 240 d
10	4	12.67	11.81	8.89	4.59	1.07	12.40	10.01	7.84	6.04	11.21	7.84	5.27	3.46
	6	8.95	13.27	11.65	8.19	3.72	13.42	12.38	10.91	9.48	13.03	10.91	8.82	7.04
	8	5.48	13.40	12.52	9.65	5.44	13.28	13.02	11.95	10.77	13.36	11.95	10.20	8.62
20	4	47.02	43.88	33.26	17.26	4.04	45.94	37.40	29.40	22.67	41.72	29.40	19.81	13.03
	6	33.66	48.87	43.53	30.87	14.09	49.12	46.06	40.88	35.67	48.17	40.88	33.21	26.58
	8	20.72	48.74	46.58	36.35	20.64	47.77	48.18	44.63	40.44	48.96	44.63	38.37	32.55
30	4	153.96	143.56	110.22	57.62	13.54	149.68	123.50	97.68	75.55	137.01	97.68	66.07	43.53
	6	113.51	157.69	144.24	104.29	48.07	157.23	151.40	136.26	119.88	156.55	136.26	111.93	90.08
	8	70.70	153.20	152.92	122.61	70.65	147.87	156.26	147.79	135.45	155.89	147.79	129.00	110.34
40	4	489.22	454.83	353.44	186.17	43.89	471.93	394.40	314.17	243.96	435.49	314.17	213.55	140.48
	6	443.68	571.38	540.94	404.51	189.74	566.48	560.66	516.22	460.70	571.33	516.22	432.36	351.58
	8	282.82	529.11	561.79	475.13	281.79	506.15	561.53	552.06	517.46	545.35	552.06	496.70	431.74

Note: $\alpha = 0.4$ m^{-1}, $\theta_s - \theta_r = 0.4$, and $m = 0$.

Table 9. Additional bearing capacity ${q_u}^{suction}$ due to transient infiltration ($q_0/k_s = 0.75$).

$\varphi'(^\circ)$	I(m)	k_s=5×10^{-6}					k_s=5×10^{-7}				k_s=5×10^{-8}			
		t = 0 d	t = 0.5 d	t = 1 d	t = 2 d	t = 4 d	t = 4 d	t = 8 d	t = 12 d	t = 16 d	t = 60 d	t = 120 d	t = 180 d	t = 240 d
10	4	12.67	12.89	11.36	8.93	6.85	13.17	11.97	10.78	9.76	12.59	10.78	9.32	8.27
	6	8.95	13.48	13.13	11.59	9.26	13.36	13.37	12.84	12.21	13.50	12.84	11.90	11.01
	8	5.48	13.09	13.46	12.49	10.51	12.72	13.48	13.33	12.94	13.31	13.33	12.72	12.04
20	4	47.02	47.43	41.83	32.68	24.78	48.41	44.09	39.67	35.83	46.35	39.67	34.17	30.18
	6	33.66	49.23	48.42	42.88	34.11	48.62	49.18	47.42	45.16	49.44	47.42	44.01	40.73
	8	20.72	47.14	49.37	46.23	38.88	45.42	49.22	49.06	47.80	48.21	49.06	47.03	44.59
30	4	153.96	153.12	134.96	104.24	77.32	156.16	142.39	127.80	114.90	149.71	127.80	109.29	95.76
	6	113.51	157.52	157.11	140.06	110.64	154.98	158.91	154.31	147.40	158.79	154.31	143.73	132.98
	8	70.70	146.81	158.54	151.03	127.22	140.14	156.68	158.52	155.60	151.47	158.52	153.43	145.97
40	4	489.22	473.14	409.64	305.36	217.45	482.97	436.21	384.38	340.81	461.71	384.38	322.08	277.35
	6	443.68	568.39	574.45	517.48	403.89	558.79	577.96	566.52	543.77	574.27	566.52	530.80	491.00
	8	282.82	507.11	567.02	558.46	473.38	482.65	552.76	573.08	570.69	526.40	573.08	565.34	542.16

Note: $\alpha = 0.4$ m^{-1}, $\theta_s - \theta_r = 0.4$, and $m = 0$.

Table 10. Additional bearing capacity ${q_u}^{suction}$ due to transient infiltration ($q_0/k_s = 0.5$).

$\varphi'(^\circ)$	I(m)	k_s=5×10^{-6}					k_s=5×10^{-7}				k_s=5×10^{-8}			
		t = 0 d	t = 0.5 d	t = 1 d	t = 2 d	t = 4 d	t = 4 d	t = 8 d	t = 12 d	t = 16 d	t = 60 d	t = 120 d	t = 180 d	t = 240 d
10	4	12.67	13.47	12.97	12.00	11.10	13.53	13.19	12.75	12.34	13.39	12.75	12.16	11.72
	6	8.95	13.00	13.51	13.39	12.74	12.74	13.40	13.54	13.50	13.19	13.54	13.45	13.25
	8	5.48	11.97	13.11	13.54	13.28	11.48	12.81	13.30	13.48	12.33	13.30	13.52	13.52
20	4	47.02	49.36	47.44	43.66	40.15	49.59	48.29	46.60	45.01	49.05	46.60	44.30	42.56
	6	33.66	47.39	49.47	49.14	46.67	46.36	49.03	49.63	49.53	48.13	49.63	49.35	48.64
	8	20.72	42.93	47.69	49.61	48.74	40.98	46.43	48.49	49.33	44.40	48.49	49.52	49.62
30	4	153.96	158.57	151.63	138.10	125.56	159.45	154.65	148.60	142.92	157.41	148.60	140.39	134.19
	6	113.51	151.69	159.17	158.54	150.08	148.25	157.48	159.90	159.76	154.23	159.90	159.23	156.88
	8	70.70	133.80	151.46	159.64	157.40	127.15	146.57	154.69	158.23	139.05	154.69	159.12	159.94
40	4	489.22	485.76	453.65	402.66	359.19	490.38	467.36	441.49	420.22	480.78	441.49	410.98	389.00
	6	443.68	550.68	577.74	575.96	540.72	539.38	571.20	580.80	580.64	559.41	580.80	578.67	569.24
	8	282.82	467.50	536.78	577.48	573.26	444.77	515.95	551.54	569.23	486.53	551.54	574.21	580.52

Note: $\alpha = 0.4$ m^{-1}, $\theta_s - \theta_r = 0.4$, and $m = 0$.

6. Conclusions

Transient infiltration, such as heavy rainfall, can lead to dramatic changes in the degree of saturation and matrix suction within the soil, thus affecting the foundation bearing capacity. In this study, a theoretical framework for considering the contribution of transient infiltration to foundation bearing capacity is provided for the first time. An analytical solution for the transient flow of linear infiltration is derived to express the soil saturation. Then, suction stress and apparent cohesion are introduced to modify the

M-C criterion. Within the framework of the kinematic approach in limit analysis, a new discrete failure mechanism suitable for considering unsaturated effects is proposed, which possesses the characteristics of fewer variables and higher accuracy. After that, the power balance equation is established, and the SQP algorithm is applied to obtain the rigorous upper-bound solution for the bearing capacity. The effectiveness and rationality of the proposed theoretical framework are fully demonstrated using comparisons with the results of previous studies and finite element results. Due to the high uncertainty in unsaturated soil properties, three hypothetical soil materials are selected for analysis. According to the comparison and parametric study, several significant conclusions are drawn as follows:

(1) Two methods for calculating the bearing capacity under transient infiltration are provided. Method 1 is an individual method, which adds an additional bearing capacity item ${q_u}^{suction}$ to the three bearing capacity items proposed by Tarzaghi and optimizes each item individually before superimposing it. Method 2 is a joint method, which directly optimizes the objective function in Equation (34) to obtain bearing capacity q_u directly. A comparison of the results shows that the upper-bound solution for method 1 is smaller than that for method 2; therefore, method 1 is more conservative. The ${q_u}^{suction}$ values under different combinations of parameters are recorded in Tables 8–10.

(2) The additional bearing capacity ${q_u}^{suction}$ due to the transient infiltration has significant temporal variability. In the initial state (t = 0), the unsaturated effect is greatest for clay, followed by silt and fine sand. For example, at l = 6 m, taking into account the effect of transient infiltration, the bearing capacity of the fine sand, silt, and clay increases by 23.60 kPa, 36.07 kPa, and 143.80 kPa, respectively. However, after a certain period of transient infiltration, the ${q_u}^{suction}$ will converge to zero for all three soils. This process takes only a few days for fine sand, tens of days for silt, and hundreds of days for clay. Notably, the speed of infiltration depends on the saturated hydraulic conductivity k_s. Increasing the value of k_s will accelerate the increase in the saturation degree and the gradual loss of apparent cohesion.

(3) The infiltration ratio q_0/k_s also has a crucial effect on the additional bearing capacity ${q_u}^{suction}$. For fine sand and silt subjected to uniform rainfall, the ${q_u}^{suction}$ increases and then decreases over time, thus presenting a clear local maximum. The maximum value occurs between 0.5 d and 1 d for fine sand and between 2 d and 4 d for silt. For the same infiltration time, a larger value of q_0/k_s means a smaller value of ${q_u}^{suction}$ in clay. The core effect of q_0/k_s on ${q_u}^{suction}$ lies its influence on the soil saturation degree S_e. The apparent cohesion increases as S_e increases from 0 to 1/e and decreases as S_e increases from 1/e to 1. Therefore, the additional bearing capacity of soil achieves its peak value at $S_e = 1/\mathrm{e}$.

Author Contributions: Methodology, S.X.; Resources, D.Z.; Data curation, S.X.; Writing—original draft, S.X.; Writing—review & editing, D.Z.; Supervision, D.Z. All authors have read and agreed to the published version of the manuscript.

Funding: This research received no external funding.

Data Availability Statement: Data available on request from the authors.

Conflicts of Interest: The authors declare no conflict of interest.

References

1. Bildik, S.; Laman, M. Experimental investigation of the effects of pipe location on the bearing capacity. *Geomech. Eng.* **2015**, *8*, 221–235. [CrossRef]
2. Fathipour, H.; Tajani, S.B.; Payan, M.; Chenari, R.J.; Senetakis, K. Impact of transient infiltration on the ultimate bearing capacity of obliquely and eccentrically loaded strip footings on partially saturated soils. *Int. J. Geomech.* **2023**, *23*, 04022290. [CrossRef]
3. Soufi, G.R.; Chenari, R.J.; Javankhoshdel, S. Conventional vs. modified pseudo-dynamic seismic analyses in the shallow strip footing bearing capacity problem. *Earthq. Eng. Eng. Vib.* **2021**, *20*, 993–1006. [CrossRef]

4. Liu, J.; Xu, S.; Yang, X.L. Modified pseudo–dynamic bearing capacity of strip footing on rock masses. *Comput. Geotech.* **2022**, *150*, 104897. [CrossRef]
5. Griffiths, D.V.; Fenton, G.A.; Manoharan, N. Bearing capacity of rough rigid strip footing on cohesive soil: Probabilistic study. *J. Geotech. Geoenvironmental Eng.* **2002**, *128*, 743–755. [CrossRef]
6. Prandtl, L. Eindringungsfestigkeit und festigkeit von schneiden. *Angew Math UMech.* **1921**, *1*, 15–20. [CrossRef]
7. Hill, R. *Mathematical Theory of Plasticity*; Clarendon Press: Oxford, UK, 1950.
8. Michalowski, R. An estimate of the influence of soil weight on bearing capacity using limit analysis. *Soils Found.* **1997**, *37*, 57–64. [CrossRef]
9. Soubra, A.-H. Upper-bound solutions for bearing capacity of foundations. *J. Geotech. Geoenvironmental Eng.* **1999**, *125*, 59–68. [CrossRef]
10. Zhu, D. The least upper-bound solutions for bearing capacity factor Nγ. *Soils Found.* **2000**, *40*, 123–129. [CrossRef]
11. Kumar, J. Effect of footing—Soil interface friction on bearing capacity factor Nγ. *Géotechnique* **2004**, *54*, 677–680. [CrossRef]
12. Kang, X.D.; Zhu, J.Q.; Yang, X.L. Seismic bearing capacity of rock foundations subjected to seepage by a unilateral piece-wise log-spiral failure mechanism. *Comput. Geotech.* **2023**, *158*, 105363. [CrossRef]
13. Oh, W.T.; Vanapalli, S.K. Interpretation of the bearing capacity of unsaturated fine-grained soil using the modified effective and the modified total stress approaches. *Int. J. Geomech.* **2013**, *13*, 769–778. [CrossRef]
14. Oh, W.T.; Vanapalli, S.K. Modelling the applied vertical stress and settlement relationship of shallow foundations in saturated and unsaturated sands. *Can. Geotech. J.* **2011**, *48*, 425–438. [CrossRef]
15. Bishop, A.W. The principal of effective stress. *Tek. Ukebl.* **1959**, *39*, 859–863.
16. Fredlund, D.G.; Morgenstern, N.R.; Widger, R.A. The shear strength of unsaturated soils. *Can. Geotech. J.* **1978**, *15*, 313–321. [CrossRef]
17. Vanapalli, S.K.; Fredlund, D.G.; Pufahl, D.E.; Clifton, A.W. Model for the prediction of shear strength with respect to soil suction. *Can. Geotech. J.* **1996**, *33*, 379–392. [CrossRef]
18. Lu, N.; Likos, W.J. *Unsaturated Soil Mechanics*; John Wiley and Sons: Hoboken, NJ, USA, 2004.
19. Lu, N.; Godt, J.W.; Wu, D.T. A closed-form equation for effective stress in unsaturated soil. A closed-form equation for effective stress in unsaturated soil. *Water Resour. Res.* **2010**, *46*, W05515. [CrossRef]
20. Griffiths, D.V.; Lu, N. Unsaturated slope stability analysis with steady infiltration or evaporation using elasto-plastic finite elements. *Int. J. Numer. Anal. Methods Geomech.* **2005**, *29*, 249–267. [CrossRef]
21. Gong, W.; Zhao, C.; Juang, C.H.; Zhang, Y.; Lu, Y. Coupled characterization of stratigraphic and geo-properties uncertainties—A conditional random field approach. *Eng. Geol.* **2021**, *294*, 106348. [CrossRef]
22. Vahedifard, F.; Leshchinsky, B.A.; Mortezaei, K.; Lu, N. Active earth pressures for unsaturated retaining structures. *J. Geotech. Geoenvironmental Eng.* **2015**, *141*, 04015048. [CrossRef]
23. Vahedifard, F.; Robinson, J.D. Unified Method for Estimating the Ultimate Bearing Capacity of Shallow Foundations in Variably Saturated Soils under Steady Flow. *J. Geotech. Geoenviron. Eng.* **2016**, *142*, 04015095. [CrossRef]
24. Tang, Y.; Taiebat, H.A.; Senetakis, K. Effective stress based bearing capacity equations for shallow foundations on unsaturated soils. *J. Geoeng.* **2017**, *12*, 59–64.
25. Du, D.; Zhuang, Y.; Sun, Q.; Yang, X.; Dias, D. Bearing capacity evaluation for shallow foundations on unsaturated soils using discretization technique. *Comput. Geotech.* **2021**, *137*, 104309. [CrossRef]
26. Xu, S.; Zhou, D. Seismic Bearing capacity solution for strip footings in unsaturated soils with modified pseudo-dynamic approach. *Mathematics* **2023**, *11*, 2692. [CrossRef]
27. Roy, S.; Chakraborty, M. Unsaturated bearing capacity of strip foundations by using the upper bound rigid block method. *Comput. Geotech.* **2023**, *156*, 105260. [CrossRef]
28. Ragno, E.; Agha Kouchak, A.; Love, C.A.; Cheng, L.; Vahedifard, F.; Lima, C.H. Quantifying changes in future intensity-duration-frequency curves using multimodel ensemble simulations. *Water Resour. Res.* **2018**, *54*, 1751–1764. [CrossRef]
29. Srivastava, R.; Yeh, T.C.J. Analytical solutions for one-dimensional, transient infiltration toward the water table in homogeneous and layered soils. *Water Resour. Res.* **1991**, *27*, 753–762. [CrossRef]
30. Li, T.Z.; Yang, X.L. New approach for face stability assessment of tunnels driven in nonuniform soils. *Comput. Geotech.* **2020**, *121*, 103412. [CrossRef]
31. Li, Z.W.; Yang, X.L. Three-dimensional active earth pressure under transient unsaturated flow conditions. *Comput. Geotech.* **2020**, *123*, 103559. [CrossRef]
32. Tan, M.; Vanapalli, S.K. Foundation bearing capacity estimation on unsaturated soil slope under transient flow condition using slip line method. *Comput. Geotech.* **2022**, *148*, 104804. [CrossRef]
33. Tan, M.; Vanapalli, S.K. Failure envelops for foundation subjected to inclined and eccentric loading considering steady state and transient flow conditions in unsaturated soils. *Comput. Geotech.* **2023**, *157*, 105315. [CrossRef]
34. Yang, X.L.; Yin, J.H. Slope stability analysis with nonlinear failure criterion. *J. Eng. Mech.* **2004**, *130*, 267–273. [CrossRef]
35. Yang, X.L.; Huang, F. Collapse mechanism of shallow tunnel based on nonlinear Hoek–Brown failure criterion. *Tunn. Undergr. Space Technol.* **2011**, *26*, 686–691. [CrossRef]
36. Yang, X.L.; Li, L.; Yin, J.H. Seismic and static stability analysis for rock slopes by a kinematical approach. *Geotechnique* **2004**, *54*, 543–549. [CrossRef]

37. Smirnov, N.N.; Nikitin, V.F.; Skryleva, E.I. Microgravity investigation of seepage flows in porous media. *Microgravity Sci. Technol.* **2019**, *31*, 629–639. [CrossRef]
38. Dushin, V.R.; Smirnov, N.N.; Nikitin, V.F.; Skryleva, E.I.; Weisman, Y.G. Multiple capillary-driven imbibition of a porous medium under microgravity conditions: Experimental investigation and mathematical modeling. *Acta Astronaut.* **2022**, *193*, 572–578. [CrossRef]
39. Smirnova, M.N.; Nikitin, V.F.; Skryleva, E.I.; Weisman, Y.G. Capillary driven fluid flows in microgravity. *Acta Astronaut.* **2023**, *204*, 892–899. [CrossRef]
40. Smirnov, N.N.; Legros, J.C.; Nikitin, V.F.; Istasse, E.; Schramm, L.; Wassmuth, F.; Hart, D.A. Filtration in artificial porous media and natural sands under microgravity conditions. *Microgravity-Sci. Technol.* **2003**, *14*, 3–28. [CrossRef]
41. Gardner, W.R. Some steady-state solutions of the unsaturated moisture flow equation with application to evaporation from a water table. *Soil Sci.* **1958**, *85*, 228–232. [CrossRef]
42. Qin, W.X.; Deng, C.X.; Hu, H.; Xiong, X.Y.; Liu, Z.C. Analytical solution of transient ultimate bearing capacity for foundation under delayed-peak pattern rainfall infiltration. *Adv. Sci. Technol. Water Resour.* **2023**, *43*, 33–38. (In Chinese)
43. Zhang, Z.L.; Yang, X.L. Unified solution of safety factors for three-dimensional compound slopes considering local and global instability. *Comput. Geotech.* **2023**, *155*, 105227. [CrossRef]
44. Zhang, Z.L.; Zhu, J.Q.; Yang, X.L. Three-dimensional active earth pressures for unsaturated backfills with cracks considering steady seepage. *Int. J. Geomech.* **2023**, *23*, 04022270. [CrossRef]
45. Xu, S.; Liu, J.; Yang, X.L. Pseudo-dynamic analysis of a 3D tunnel face in inclined weak strata. *Undergr. Space* **2023**, *12*, 156–166. [CrossRef]
46. Chen, B.H.; Luo, W.J.; Xu, X.Y.; Hu, R.Q.; Yang, X.L. Seismic bearing capacity of strip footing with nonlinear Mohr–Coulomb failure criterion. *Int. J. Geomech.* **2022**, *22*, 06022029. [CrossRef]
47. Zhong, J.H.; Yang, X.L. Kinematic analysis of the three-dimensional stability for tunnel faces by pseudodynamic approach. *Comput. Geotech.* **2021**, *128*, 103802. [CrossRef]
48. Yang, X.L.; Wang, J.M. Ground movement prediction for tunnels using simplified procedure. *Tunn. Undergr. Space Technol.* **2011**, *26*, 462–471. [CrossRef]
49. Yang, X.L.; Yin, J.H. Upper bound solution for ultimate bearing capacity with a modified Hoek-Brown failure criterion. *Int. J. Rock Mech. Min. Sci.* **2005**, *42*, 550–560. [CrossRef]
50. Jin, L.; Zhang, H.; Feng, Q. Ultimate bearing capacity of strip footing on sands under inclined loading based on improved radial movement optimization. *Eng. Optim.* **2021**, *53*, 277–299. [CrossRef]
51. Wang, Y.J.; Yin, J.H.; Chen, Z.Y. Calculation of bearing capacity of a strip footing using an upper bound method. *Int. J. Numer. Anal. Methods Geomech.* **2001**, *25*, 841–851. [CrossRef]
52. Vesic, A.S. *Bearing Capacity of Shallow Foundations, Foundation Engineering Handbook*; Winterkorn, F.S., Fand, H.Y., Eds.; Springer: Berlin/Heidelberg, Germany, 1975.
53. Chen, W.F. *Limit Analysis and Soil Plasticity*; Elsevier: Amsterdam, The Netherlands, 1975.
54. Zhong, J.; Hou, C.; Yang, X. Bearing capacity of foundations resting on rock masses subjected to Rayleigh waves. *Soil Dyn. Earthq. Eng.* **2023**, *167*, 107791. [CrossRef]